

# Retrieval of near-surface sulfur dioxide (SO2) concentrations at a global scale using IASI satellite observations

Sophie Bauduin, Lieven Clarisse, Juliette Hadji-Lazaro, Nicolas Theys, Cathy Clerbaux, Pierre-François Coheur

▶ **To cite this version:**

Sophie Bauduin, Lieven Clarisse, Juliette Hadji-Lazaro, Nicolas Theys, Cathy Clerbaux, et al.. Retrieval of near-surface sulfur dioxide (SO2) concentrations at a global scale using IASI satellite observations. Atmospheric Measurement Techniques, 2016, 9 (2), pp.721-740. 10.5194/amt-9-721-2016 . insu-01220703

**HAL Id: insu-01220703**

**https://insu.hal.science/insu-01220703**

Submitted on 29 Feb 2016

**HAL** is a multi-disciplinary open access archive for the deposit and dissemination of scientific research documents, whether they are published or not. The documents may come from teaching and research institutions in France or abroad, or from public or private research centers.

L'archive ouverte pluridisciplinaire **HAL**, est destinée au dépôt et à la diffusion de documents scientifiques de niveau recherche, publiés ou non, émanant des établissements d'enseignement et de recherche français ou étrangers, des laboratoires publics ou privés.

Atmos. Meas. Tech., 9, 721–740, 2016
www.atmos-meas-tech.net/9/721/2016/
doi:10.5194/amt-9-721-2016
© Author(s) 2016. CC Attribution 3.0 License.



Atmospheric Measurement Techniques
Open Access
EGU

# Retrieval of near-surface sulfur dioxide ($SO_2$) concentrations at a global scale using IASI satellite observations

**Sophie Bauduin[1], Lieven Clarisse[1], Juliette Hadji-Lazaro[2], Nicolas Theys[3], Cathy Clerbaux[1,2], and Pierre-François Coheur[1]**

[1]Spectroscopie de l'atmosphère, Service de Chimie Quantique et Photophysique, Université Libre de Bruxelles (ULB), Brussels, Belgium
[2]Sorbonne Universités, UPMC Univ. Paris 06, Université Versailles St-Quentin, CNRS/INSU, LATMOS-IPSL, Paris, France
[3]Belgian Institute for Space Aeronomy (BIRA-IASB), Brussels, Belgium

*Correspondence to:* Sophie Bauduin (sbauduin@ulb.ac.be)

Received: 25 August 2015 – Published in Atmos. Meas. Tech. Discuss.: 26 October 2015
Revised: 9 February 2016 – Accepted: 10 February 2016 – Published: 29 February 2016

**Abstract.** $SO_2$ from volcanic eruptions is now operationally monitored from space in both the ultraviolet (UV) and thermal infrared (TIR) spectral range, but anthropogenic $SO_2$ has almost solely been measured from UV sounders. Indeed, TIR instruments are well known to have a poor sensitivity to the planetary boundary layer (PBL), due to generally low thermal contrast (TC) between the ground and the air above it. Recent studies have demonstrated the capability of the Infrared Atmospheric Sounding Interferometer (IASI) to measure near-surface $SO_2$ locally, for specific atmospheric conditions. In this work, we develop a retrieval method allowing the inference of $SO_2$ near-surface concentrations from IASI measurements at a global scale. This method consists of two steps. Both are based on the computation of radiance indexes representing the strength of the $SO_2$ $\nu_3$ band in IASI spectra. The first step allows the peak altitude of $SO_2$ to be retrieved and near-surface $SO_2$ to be selected. In the second step, 0–4 km columns of $SO_2$ are inferred using a look-up table (LUT) approach. Using this new retrieval method, we obtain the first global distribution of near-surface $SO_2$ from IASI-A, and identify the dominant anthropogenic hotspot sources and volcanic degassing. The 7-year daily time evolution of $SO_2$ columns above two industrial source areas (Beijing in China and Sar Cheshmeh in Iran) is investigated and correlated to the seasonal variations of the parameters that drive the IASI sensitivity to the PBL composition. Apart from TC, we show that humidity is the most important parameter which determines IR sensitivity to near-surface $SO_2$ in the $\nu_3$ band. As IASI provides global measurements twice daily, the differences between the retrieved columns for the morning and evening orbits are investigated. This paper finally presents a first intercomparison of the measured 0–4 km columns with an independent iterative retrieval method and with observations of the Ozone Monitoring Instrument (OMI).

## 1 Introduction

Sulfur dioxide ($SO_2$) is an atmospheric trace gas with both natural and anthropogenic sources. Volcanic emissions are the largest natural contributors to tropospheric and stratospheric $SO_2$, and account for 7.5–10.5 Tg of S per year on average (Andres and Kasgnoc, 1998; Halmer et al., 2002). Anthropogenic sources emit on average 60–100 Tg of S per year (Stevenson et al., 2003), with the major contribution coming from combustion of sulfur-rich fuels, such as coal and oil, and smelting of heavy metals (Smith et al., 2011). The sinks of $SO_2$ are dry (Wesely, 2007) and wet (Ali-Khodja and Kebabi, 1998) deposition, and oxidation by the OH radical in the gas phase or by $O_3$ and $H_2O_2$ in the aqueous phase (Eisinger and Burrows, 1998; Stevenson et al., 2003). The $SO_2$ lifetime varies according to the sinks from a few hours to several days in the lower troposphere (Lee et al., 2011).

$SO_2$ emissions of most volcanoes are now well monitored from space, especially eruptive degassing. Significant amounts of $SO_2$ are in this case mainly injected in the high troposphere or stratosphere and cover large ar-

eas. In the ultraviolet (UV) spectral range, retrievals of volcanic $SO_2$ began in 1978 using the Total Ozone Mapping Spectrometer (TOMS) instrument (Krueger, 1983; Carn et al., 2003) and have continued since then using the Global Ozone Monitoring Experiment (GOME) (Eisinger and Burrows, 1998), SCanning Imaging Absorption spectroMeter for Atmospheric CHartographY (SCIAMACHY) (Lee et al., 2008), GOME-2 (Rix et al., 2009) and Ozone Monitoring Instrument (OMI) (Krotkov et al., 2006). In the thermal infrared (TIR) spectral range, volcanic $SO_2$ was measured by multi-channel instruments with moderate resolution (e.g. Realmuto and Watson, 2001; Watson et al., 2004) and later using high-spectral resolution instruments such as Tropospheric Emission Spectrometer (TES) (Clerbaux et al., 2008), Atmospheric Infrared Sounder (AIRS) (Carn et al., 2005) and Infrared Atmospheric Sounding Interferometer (IASI) (Clarisse et al., 2008).

In contrast to volcanoes, $SO_2$ pollution from anthropogenic activities is difficult to monitor because it is often confined horizontally and vertically. In the UV spectral range, different methods have successfully been developed to retrieve surface $SO_2$. These are included in different global products such as the operational planetary boundary layer (PBL) OMI $SO_2$ product (Krotkov et al., 2006, 2008) or the recent OMI algorithm based on a multi-windows Differential Optical Absorption Spectroscopy (DOAS) scheme developed by Theys et al. (2015). The latter will be used for comparison purposes later in this paper. The availability of the satellite-derived columns from the UV nadir sounders have allowed $SO_2$ anthropogenic emissions to be inferred (e.g. Carn et al., 2007; Fioletov et al., 2011, 2013, 2015; McLinden et al., 2012, 2014). This has not yet been possible using TIR instruments, which suffer from lower sensitivity to the near-surface atmosphere due to generally low temperature differences between the surface and the PBL atmosphere (hereafter called thermal contrast). Recently Bauduin et al. (2014) and Boynard et al. (2014) have nevertheless demonstrated the capability of IASI to measure near-surface $SO_2$ locally. Both studies revealed that the presence of large thermal inversions (associated to high negative thermal contrasts) and low humidity (preventing opacity in the $\nu_3$ band) has allowed near-surface $SO_2$ to be retrieved. However, the detection of $SO_2$ by IASI could theoretically be achieved in other situations, particularly in the case of large positive thermal contrasts, which correspond to a surface much hotter than the atmosphere. This is demonstrated and discussed in Sect. 3, which provides the first global distributions of near-surface $SO_2$ from IASI over the period 2008–2014. The method used to retrieve $SO_2$ columns, described thoroughly in Sect. 2, relies on the calculation of a hyperspectral range index (HRI), similarly to the work of Van Damme et al. (2014) for ammonia ($NH_3$). As the aim of this work is to retrieve near-surface $SO_2$, the determination of the altitude of $SO_2$ defines the first step of the method and relies on the work of Clarisse et al. (2014). It is used to remove all plumes located above a height of 4 km, which likely correspond to volcanic eruptions. The retrieval of 0–4 km $SO_2$ columns is performed in a second step, where calculated HRIs are converted into columns using a look-up table (LUT) approach. This calculation is performed using the $\nu_3$ band (1300–1410 $cm^{-1}$). This spectral band has the advantage of being more intense than the $\nu_1$ band (a factor of 7.8 larger for the strongest lines, Bauduin et al., 2014). It is however more affected by the absorption of $H_2O$, which can cause opacity in this spectral region in the near-surface atmosphere and therefore can reduce the IASI sensitivity to $SO_2$ down to the surface. This parameter, along with thermal contrast, has been taken into account in the whole retrieval procedure (described in Sect. 2) and the results are analysed with respect to these two parameters.

## 2 $SO_2$ near-surface product

### 2.1 IASI and methodology

The IASI instrument is a Michelson interferometer onboard MetOp platforms (A and B) circling the Earth on a Sun-synchronous polar orbit. The IASI effective field of view is composed of $2 \times 2$ footprints, each with a diameter of 12 km at nadir. IASI has global coverage twice a day thanks to a swath of 2200 km and two overpasses per day (morning at 09:30 LT and evening at 21:30 LT at the equator). The instrument covers the thermal infrared spectral range from 645 to 2760 $cm^{-1}$ with a spectral resolution of 0.5 $cm^{-1}$ after apodization. Each measurement consists of 8461 radiance channels (0.25 $cm^{-1}$ sampling) and is characterized by a noise of 0.2 K on average. Details about the instrument can be found elsewhere (Clerbaux et al., 2009; Hilton et al., 2012). Only measurements of the IASI-A instrument have been considered here.

The methodology used in this work to retrieve near-surface $SO_2$ amount relies on the sensitive detection method of trace gases introduced by Walker et al. (2011), and used later by Van Damme et al. (2014) for retrieving $NH_3$ columns at a global scale from IASI. Retrieval approaches based on spectral fitting generally consist of simultaneous iterative adjustments of the atmospheric parameters of interest (here the 0–4 km $SO_2$ column) and spectrally interfering unknown variables. The idea of the proposed method is to consider the interfering variables as permanent unknowns and to incorporate them in a generalized noise covariance matrix **S**. This matrix should include all variability coming from the parameters affecting the IASI spectrum in the spectral range under consideration (here 1300–1410 $cm^{-1}$, corresponding to the $\nu_3$ band) but not $SO_2$. In this way, instead of iteratively adjusting the $SO_2$ columns and the interfering parameters, a normalized range index is calculated according to

$$\mathrm{HRI} = \frac{\boldsymbol{K}^T \mathbf{S}^{-1}(\boldsymbol{y} - \overline{\boldsymbol{y}})}{\sqrt{\boldsymbol{K}^T \mathbf{S}^{-1} \boldsymbol{K}}}, \quad (1)$$

where $\boldsymbol{K}$ is a Jacobian, a derivative of the IASI spectrum $\boldsymbol{y}$ with respect to $SO_2$; $\overline{\boldsymbol{y}}$ is the mean background spectrum with no detectable $SO_2$ associated with the matrix **S**. This matrix **S** acts as a weight in the projection of the observed spectrum onto the $SO_2$ signature, giving more importance to IASI channels less influenced by interfering parameters. Practically, $\overline{\boldsymbol{y}}$ and **S** are built from a sufficiently large sample of $SO_2$-free IASI spectra to include the global atmospheric variability in the absence of $SO_2$ (see Sects. 2.2 and 2.3).

The HRI, which is unitless, can be seen as an index of detection, whose value represents the strength of the $SO_2$ signal in the IASI radiance spectrum, which is related to the amount of $SO_2$ in the atmosphere. The larger its value, the more likely the enhancement of the gas. An ensemble of $SO_2$-free spectra has a mean HRI of 0 and a standard deviation of 1, and a HRI of 3 (which corresponds to $3\sigma$) can reasonably be considered as the limit of detection. Because the HRI does not correspond to the real column of $SO_2$, it is therefore needed to convert it in a subsequent step. This can be done by using look-up tables built from forward model simulations, which link the simulated HRI values to known $SO_2$ columns. Prior to this, as this work focuses on near-surface pollution, we use the algorithm of Clarisse et al. (2014) to select the spectra with detectable low-altitude $SO_2$ enhancements. Only plumes located below 4 km are kept. These successive steps of the retrieval scheme are detailed in the next sections.

### 2.2 Retrieval of the altitude of the plume

The altitude of $SO_2$ is retrieved using the algorithm presented in Clarisse et al. (2014). In short, a HRI is computed for different altitudes following

$$\mathrm{HRI}(h) = \frac{\boldsymbol{K}_h^T \mathbf{S}^{-1}(\boldsymbol{y} - \overline{\boldsymbol{y}})}{\sqrt{\boldsymbol{K}_h^T \mathbf{S}^{-1} \boldsymbol{K}_h}}, \quad (2)$$

where the $\boldsymbol{K}_h$ is the Jacobian for $SO_2$ located at an altitude $h$. If there is a detectable amount of $SO_2$, the function HRI($h$) will peak at the altitude of the plume. Indeed, the overlap between the IASI spectrum and the $SO_2$ spectral signature is maximal at this altitude. The height determination therefore consists in calculating the function HRI($h$) at predefined altitudes and finding the altitude of its maximum.

To this end, $\boldsymbol{K}_h$ Jacobians have been precalculated using the finite difference method for the spectral range 1300–1410 $\mathrm{cm}^{-1}$ using monthly averaged $H_2O$ and temperature profiles in $10^\circ \times 20^\circ$ boxes. These averages were calculated from the meteorological fields from the EUMETSAT L2 Product Processing Facility (PPF) (Schlüssel et al., 2005; August et al., 2012) using the 15th of each month of 2009, 2011 and 2013. One set of 30 vectors $\boldsymbol{K}_h$ has been generated for each box and for each month, considering a 1 km thick $SO_2$ layer of 5 DU (1 Dobson unit $= 2.69 \times 10^{16}$ molecules $\mathrm{cm}^{-2}$), located every 1 km from 1 to 30 km. For each IASI observation, local Jacobians are then calculated using a bilinear interpolation of the four closest grid boxes, to better take the variation of the atmospheric conditions into account when observations move away from the centre of the boxes. The mean background spectrum $\overline{\boldsymbol{y}}$ and the associated covariance matrix **S** needed to calculate the HRI (Eq. 2) have been built using a sample of 1 million randomly chosen IASI spectra. Those with detectable $SO_2$ have been filtered out using an iterative approach: first, spectra with observable $SO_2$ signatures were rejected using a brightness temperature difference method (see Clarisse et al. (2008) for details) and a first estimate of the matrix **S** was made. The second step uses this initial matrix to exclude spectra with measurable HRI from the remaining set of measurements (a similar method is used in Van Damme et al., 2014 and Clarisse et al., 2013). Similarly to the Jacobians, $\overline{\boldsymbol{y}}$ and **S** are calculated over the spectral range 1300–1410 $\mathrm{cm}^{-1}$. Note that an altitude was retrieved when an HRI larger than 2 was found, even though in practice we expect the altitude retrieval to be accurate only for HRI values above 4 or 5.

As explained in Clarisse et al. (2014), because of the use of averaged Jacobians, the retrieved altitude can be biased, especially close to the surface. The best accuracy is achieved between 5 and 15 km, and the altitude estimate is provided within 1–2 km. Below 5 km, the retrieved altitude is more uncertain. However, this is not an important issue here as the altitude is used only to filter out $SO_2$ plumes emitted by volcanoes directly in the free troposphere. In the following, only plumes located between the surface and 4 km above ground are selected. The retrieved $SO_2$ corresponds therefore to a 4 km thick layer (hereafter called 0–4 km column).

From the calculated $\boldsymbol{K}_h$, we can estimate where in the retrieved 0–4 km layer IASI is the most sensitive to $SO_2$. We found that, for favourable conditions of thermal contrast and humidity, IASI is sensitive down to the surface but has its maximum sensitivity in the upper part of the 0–4 km layer. In the case of low thermal contrast (TC) and/or large column of $H_2O$, IASI becomes insensitive to the lower part of the 0–4 km layer.

### 2.3 Retrieval of near-surface $SO_2$ concentrations – look-up tables

For the low $SO_2$ plumes, the next step consists in computing a HRI (according to Eq. 1) for each IASI measurement and converting it to a $SO_2$ column. Different Jacobian $\overline{\boldsymbol{y}}$ and **S** have been built for this second step (see section below). Because a constant Jacobian is used in the calculation of the HRI, there are several parameters that impact its value in addition to the $SO_2$ abundance itself and they need to be ac-

counted for. We have considered the impact of viewing angle (by building angle-dependent matrices for the HRI calculation – see Sect. 2.3.1) and the impact of humidity and thermal contrast, which are separate entries in the look-up tables (Sect. 2.3.2).

### 2.3.1 Angular dependency

The dependence of the signal strength on the viewing angle has to be taken into account in the conversion of HRI values. As reported by Van Damme et al. (2014), the application of a cosine factor to account for the increased path length tends to overcorrect the HRI and leads to a bias for larger angles. As they suggested, angle-dependent $\boldsymbol{K}$, $\overline{\boldsymbol{y}}$ and $\mathbf{S}$ have been used. Specifically, between 0 and 55°, 5° angle bins have been defined and a last one of 4° is considered for 55–59° (IASI zenith angle ranges between 0 and 58.8°). For the median angle of each bin, a Jacobian has been generated for a standard atmosphere (Anderson et al., 1986), with a scaling factor applied to the methane profile according to Bauduin et al. (2014). A thermal contrast of 10 K has been considered. All $\boldsymbol{K}$ values have been calculated with the finite difference method for 200 ppb $SO_2$ well mixed between 4 and 5 km, and over the 1300–1410 $cm^{-1}$ range. For $\overline{\boldsymbol{y}}$ and $\mathbf{S}$, almost the totality of cloud-free (i.e. cloud fraction below 20 % and available EUMETSAT L2 surface temperature, atmospheric temperature and $H_2O$ profiles) observations of the 15th of each month of 2009 and 2011 have been used, sorted by angle bins. Measurements with detectable $SO_2$ have been filtered as above. In this way, for each angle bin, $\overline{\boldsymbol{y}}$ and $\mathbf{S}$ have been calculated from about 750 000 spectra.

### 2.3.2 Look-up tables

The conversion of the HRI into an $SO_2$ column is done using look-up tables, which, as for $\overline{\boldsymbol{y}}$ and $\mathbf{S}$, have been separated per angle bin. The LUTs include four dimensions linking thermal contrast, total column of water, HRI and $SO_2$ column. To build the LUT, forward simulations of IASI spectra have been performed for a series of situations, summarized in Table 1, using the line-by-line Atmosphit software (Coheur et al., 2005). More specifically, the following parameters were varied to provide a representative set of atmospheric conditions.

- *$SO_2$ columns*: to obtain a reference $SO_2$ vertical profile for anthropogenic emissions, we relied on the global chemistry transport MOZART model (Emmons et al., 2010) outputs of January, April, July and October 2009 and 2010. An average profile was calculated from all modelled profiles above the eastern United States, Europe and eastern China, with the $SO_2$ concentration above 4 km set to zero. The resulting reference profile is shown in Fig. 1 (blue). The set of atmospheric $SO_2$ columns included in the LUT was then obtained by scaling this reference profile by the 16 factors listed in Table 1, leading to a range of 0–4 km $SO_2$ columns (ground to 4 km above it) going from 0 to 415 DU.

- *$H_2O$*: in a similar way, the water vapour profile from the US Standard model (Fig. 1 in red) has also been varied using 16 scaling factors (Table 1), covering a range of $H_2O$ total column from $9.5 \times 10^{19}$ to $2.3 \times 10^{23}$ molecules $cm^{-2}$.

- *Temperature*: a single temperature profile has been used (US standard, Fig. 1, right panel). To include a range of thermal contrast values, which are defined as the difference between the temperature of the ground and the temperature of the air at 500 m (see Fig. 1), we have varied the surface temperature to provide 25 different situations, listed in Table 1. These include extreme cases of thermal contrasts, from −30 to +40 K, but also a range of low and moderate values. Note that a thermal contrast of 0 corresponds to an isothermal 0–1 km layer and implies that the outgoing radiance of this layer is that of a black body (Bauduin et al., 2014). Note also that a constant emissivity of 0.98 has been used in the forward simulations; for most cases, differences between using a spectrally varying emissivity and a constant emissivity are on the order of the noise of the instrument.

The LUTs constructed as described above have been interpolated on a finer grid (TC, $H_2O$ and $SO_2$ dimensions). An example of resulting LUT is shown in Fig. 2a (for constant water vapour) and Fig. 2b (for constant thermal contrast). The retrieval scheme consists in determining, for each IASI measurement, the satellite zenith angle, the HRI, the thermal contrast, the total column of water vapour and, using the LUT, the 0–4 km column of $SO_2$.

From Fig. 2, it can be seen that the HRI has the same sign as the thermal contrast. In the case of positive thermal contrast, this is explained by the fact that $SO_2$ spectral lines are in absorption in IASI measurements, resulting in a negative difference ($\boldsymbol{y} - \overline{\boldsymbol{y}}$). Given the fact that the Jacobians are also negative (see definition in Sect. 2.3.1), the calculated HRI is positive. As a rule, for constant zenith angle, $H_2O$ column and $SO_2$ column, the value of the HRI increases with the thermal contrast. This increase in spectral signal corresponds to an increase of IASI sensitivity to near-surface $SO_2$. However (see Fig. 2b for a constant TC of 15 K), for increasing water vapour, which renders the atmosphere opaque in the low layers, the IASI sensitivity decreases along with the HRI for constant $SO_2$ columns, thermal contrast and viewing angle. In the case of negative thermal contrast, $SO_2$ lines are in emission and the calculated HRI is negative too. For decreasing negative thermal contrast, the HRI value usually decreases. But from Fig. 2a it can be seen that some HRI values are positive for negative thermal contrasts. We explored this seemingly odd behaviour with the help of Fig. 3 (left panel), which shows HRI as a function of $SO_2$ for a thermal contrast of −10 K and a total column of $H_2O$ of

**Table 1.** Range of atmospheric situations considered for the forward model runs used as reference for the LUTs.

| | Reference profile[1] | Range of values[3] |
|---|---|---|
| $SO_2$ | MOZART average for polluted conditions up to 4 km; 0 above | Multiplicative factor applied on the entire reference profile: 0, 1, 5, 10, 15, 20, 30, 40, 50, 80, 100, 160, 240, 320, 640 and 1000 |
| $H_2O$ | US Standard model | Multiplicative factor applied on the entire reference profile: 0.002, 0.005, 0.01, 0.05, 0.1, 0.2, 0.5, 1, 1.5, 1.8, 2, 2.5, 3, 3.5, 4 and 5 |
| Thermal contrast[2] | Temperature profile from US Standard model | −30, −25, −20, −17, −15, −12, −10, −7, −5, −3, 0, 3, 5, 7, 10, 12, 15, 17, 20, 22, 25, 27, 30, 35, 40 |

[1] The reference profiles for $SO_2$, $H_2O$ and temperature are shown in Fig. 1. [2] Thermal contrast defined as the difference between the surface temperature (variable) and the temperature of the air at 500 m (from the reference profile). [3] In degrees for the thermal contrast; unit less for $SO_2$ and $H_2O$ scaling factors.

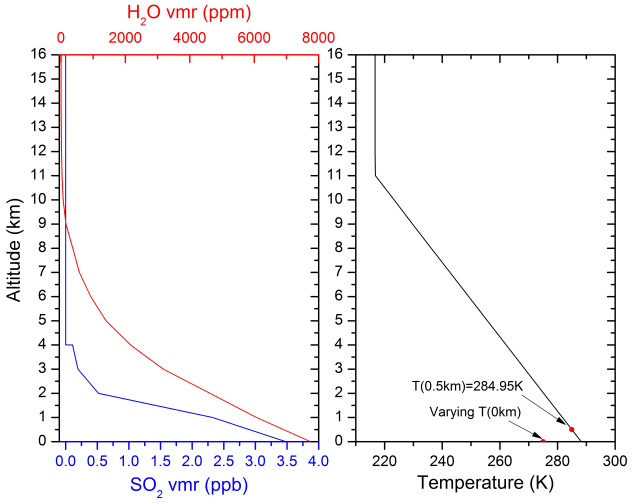



**Figure 1.** The 2-year average $SO_2$ vertical profile (ppb, blue) calculated from MOZART simulations (2009–2010), US Standard water vapour profile (ppm, red) and temperature (K, right panel). The $SO_2$ profile shown here corresponds to a 0–4 km column of $SO_2$ of 0.4 DU. The thermal contrast is defined as the difference between the surface temperature and the temperature of the air at 500 m (red dots).

$2.4 \times 10^{20}$ molecules $cm^{-2}$. From 0 to 66.33 DU, HRI decreases for increasing $SO_2$. Above 66.33 DU, the HRI starts to increase with increasing $SO_2$. From about 250 DU, the HRI becomes positive. This behaviour can be explained by the competition between emission (mainly in the 0–1 km layer) and absorption (above 1 km). Figure 3 (right panel) presents the contributions (in absolute value) of the emission in the 0–1 km layer and the absorption in the 1–4 km layer to the total spectral signal as a function of the 0–4 km $SO_2$ column. They have been evaluated at 1355 $cm^{-1}$ using similar techniques as in Clarisse et al. (2010). In Fig. 3, for concentrations ranging from 0 to 66.33 DU, emission in the 0–1 km layer increases more rapidly than absorption in the 1–4 km layer. This results in decreasing HRI (more and more negative). From 66.33 DU, emission comes closer to saturation; its increase is slower than the one of absorption, whose saturation occurs for larger $SO_2$ columns, and the HRI begins to increase. From around 250 DU, absorption totally counterbalances emission and HRI values become positive. This competition between emission in the lowest layers and absorption higher up depends on the value of the temperature inversion, as the latter determines the strength of the emission. Note that this competition also depends on the altitude of the thermal inversion, but which is constant here (just above the ground). The consequence is that, for negative thermal contrast, a negative HRI can be converted into two $SO_2$ columns (see Fig. 3, left panel): a small one (emission combined with lower absorption above 1 km) and a large one (larger emission partly counterbalanced by a more rapid increase of absorption above 1 km). In that case, because the very large columns included in the LUTs are not expected above anthropogenic sources, only the smallest one is considered. Note that the large columns for which the HRI is positive for negative thermal contrast have been kept.

From the LUT, we can estimate the detection limit of IASI to near-surface $SO_2$. In Fig. 4, the lowest detectable 0–4 km column of $SO_2$ is presented as a function of thermal contrast and the total column of $H_2O$. These columns have been calculated using the LUT assuming a detection threshold of 3 on the value of HRI (see Sect. 2.1). As expected, this limit of detection largely depends on thermal contrast and humidity. Indeed, when the former is close to 0, IASI stays insensitive, even to large $SO_2$ columns. For large thermal contrasts, 0–4 km columns lower than 1 DU can be measured. This also depends on the humidity. Below $2 \times 10^{22}$ molecules $cm^{-2}$, the limit of detection stays below 2 DU for both high positive and high negative thermal contrasts. For larger $H_2O$ amount,

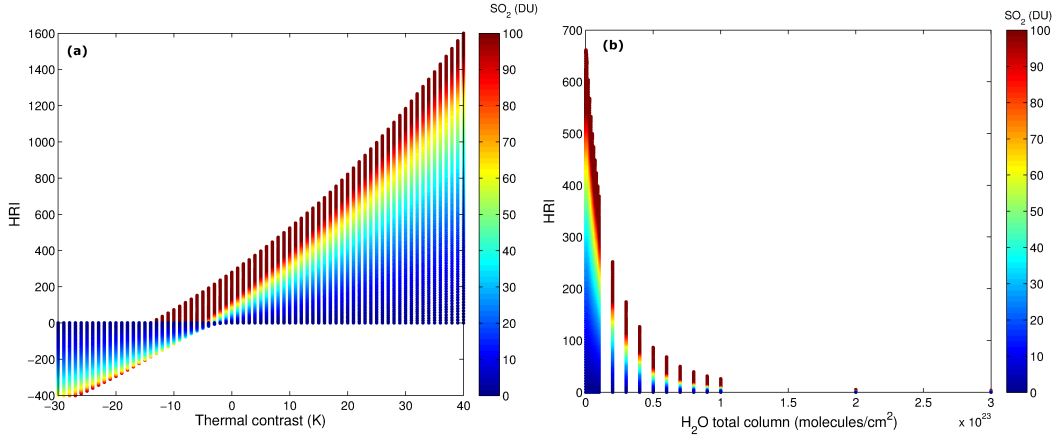



**Figure 2.** Example of interpolated LUT to convert HRI in $SO_2$ column depending on thermal contrast and water vapour for the angle bin 15–20°. The colour bar represents the 0–4 km column of $SO_2$ in DU. Panel **(a)** shows the dependency of HRI on thermal contrast (constant total column of $H_2O$ of $2 \times 10^{20}$ molecules $cm^{-2}$); panel **(b)** shows the dependency on the total column of water (constant thermal contrast of 15 K).

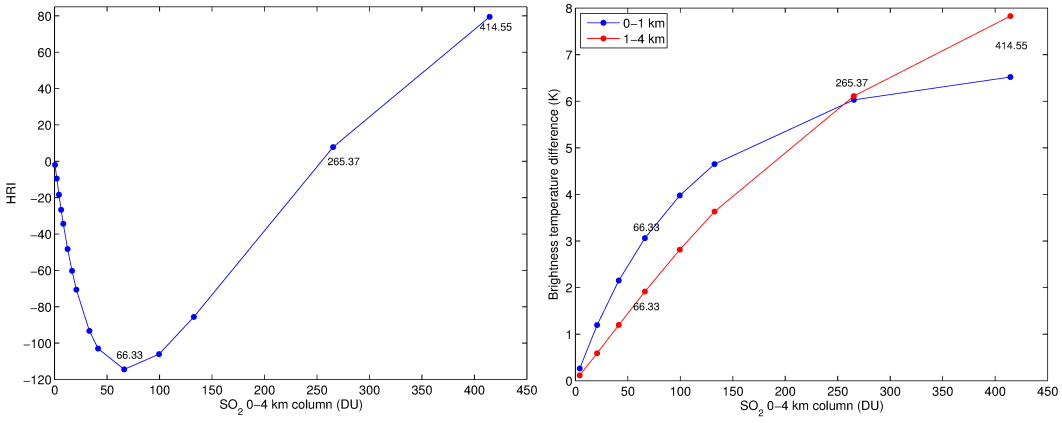



**Figure 3.** Left panel: evolution of the HRI as a function of the 0–4 km column of $SO_2$, in the case of negative thermal contrast (−10 K). In this simulation, the total $H_2O$ column is $2.4 \times 10^{20}$ molecules $cm^{-2}$ and the angle bin is 15–20°. Right panel: contributions of the emission in the 0–1 km layer (blue) and of absorption in the 1–4 km layer (red) to the IASI spectrum at 1355 $cm^{-1}$, expressed in brightness temperature difference (absolute value). Details are given in the text.

this limit rapidly increases for negative thermal contrast but stays relatively low for large positive thermal contrasts. From above $4 \times 10^{22}$ molecules $cm^{-2}$ of $H_2O$, the detection threshold starts to increase for positive thermal contrasts.

### 2.3.3 Error characterization

For each LUT, an associated table of errors has been generated by propagating the uncertainties of the different LUT parameters:

$$\sigma_{SO_2} = \sqrt{\left(\frac{\partial SO_2}{\partial TC}\right)^2 \sigma_{TC}^2 + \left(\frac{\partial SO_2}{\partial H_2O}\right)^2 \sigma_{H_2O}^2 + \left(\frac{\partial SO_2}{\partial HRI}\right)^2 \sigma_{HRI}^2}, \quad (3)$$

where $\sigma_{SO_2}$ is the absolute error of the $SO_2$ column, $\sigma_{TC}$ and $\sigma_{H_2O}$ are the errors on thermal contrast and total column of water vapour, which are respectively taken equal to $\sqrt{2}$ K and 10 %, relying on early validation of the IASI level 2 meteorological fields from the PPF (Pougatchev et al., 2009); $\sigma_{HRI}$ is the standard deviation of the HRI and is equal to 1.

An example of error tables is given in Fig. 5 (Fig. 5a relative errors and Fig. 5b absolute error) for the angle bin 0–5° and for a total column of water vapour of $2 \times 10^{20}$ molecules $cm^{-2}$. As expected, the errors are directly linked to the IASI sensitivity to near-surface $SO_2$, with large errors (above 100 % and 10 DU respectively for relative and absolute errors) occurring in the case of small thermal contrasts. The errors decrease with increasing thermal contrasts and drop to 20 % (2 DU) or less in the most favourable situations. As discussed above, for large total columns of $H_2O$, IASI is also less sensitive to near-surface $SO_2$ and errors in-

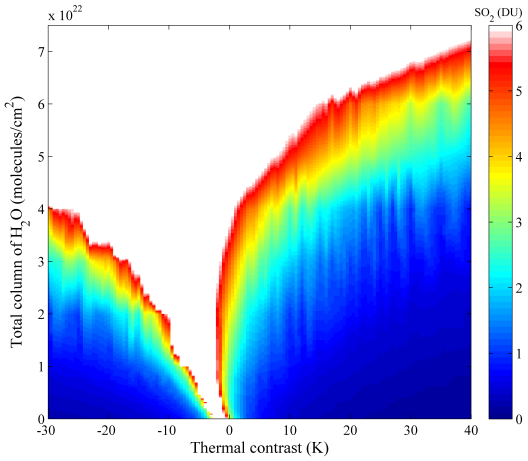



**Figure 4.** Lowest detectable 0–4 km $SO_2$ column (colour bar, in DU) as a function of the thermal contrast and the total column of $H_2O$ for the angle bin 15–20°. These columns correspond to a HRI of 3 ($3\sigma$), which can be considered as the detection threshold.

crease accordingly. The errors are used in the following to filter out the data (see Sect. 3).

Another source of errors, which is not taken into account in the error calculation, is the assumed $SO_2$ vertical profile. A given column amount of $SO_2$ located at different altitudes corresponds to different HRI values. For instance, we have estimated the error on the $SO_2$ column to be of the order of 30 % when $SO_2$ is confined to the 0–1 km layer only (for a TC of 10 K and a total column of $H_2O$ of $9.5 \times 10^{21}$ molecules $cm^{-2}$). Note also that the assumed temperature profile can be a source of error (see Sect. 3.3).

## 3 Results

In this section, global distributions, time series and a first product evaluation are presented. For this, only $SO_2$ columns with less than 25 % relative error and less than 10 DU in absolute error have been used. The second criterion was necessary to remove spurious data over the cold Antarctic region with unrealistic high columns. The first condition has been chosen to reject measurements for which IASI sensitivity to near-surface $SO_2$ is limited, and thus for which associated retrieved $SO_2$ columns have large uncertainties. However, this procedure tends to favour large $SO_2$ columns. As a consequence, the presented averages are expected to be biased high. It is important to stress though that individual measurements that pass the filter are not a priori biased but have random uncertainties related to errors on the different input parameters (errors on TC, choice of temperature and $SO_2$ profile). It is also important to note that by using the HRI > 2 criterion early in the retrieval procedure, we have made the choice not to treat observations with small or undetectable amounts of $SO_2$. This potentially throws away one category of useful observations: those where a low HRI is found together with favourable atmospheric conditions. In this case, a low HRI can be an indication of the absence of large $SO_2$ concentrations at the surface. Future versions of the retrieval algorithm could be expanded to include those, and this would potentially decrease the high bias when calculating averages.

### 3.1 Global distributions

The $SO_2$ retrievals have been performed on 7 years of IASI observations (1 January 2008–30 September 2014). In Fig. 6, an average global distribution of the near-surface column of $SO_2$ for this period is presented, separately for day (top panel) and night (bottom panel) observations. Only measurements with less than 20 % cloud fraction in the IASI field of view and with available surface temperature, profiles of temperature and $H_2O$ from the EUMETSAT IASI level 2 PPF have been used. A selection based on the error, described in the beginning of Sect. 3, has also been applied. The columns that pass these posterior filters have been averaged on a $0.5° \times 0.5°$ grid for cells including more than five IASI measurements. The bottom-right inset in the daytime map presents the total number of successful measurements (those which pass the error filtering) in each grid boxes. The bottom-right inset in the night-time map presents the global anthropogenic emissions (in kg $s^{-1}$ $m^{-2}$) of $SO_2$ provided by the EDGAR v4.2 inventory (downloaded from the ETHER/ECCAD database) (EDGAR-Emission Database for Global Atmospheric Research, 2011).

Figure 6 reveals several anthropogenic and volcanic hotspots, numbered from 1 to 13. Most of them are observed during the morning overpass, when the thermal contrast is large. They are detailed here.

1. *China*: China is one of the world's largest emission sources of $SO_2$, mainly due to energy supply through coal combustion (Lu et al., 2010; Smith et al., 2011; Lin et al., 2012). A large region of enhanced $SO_2$ columns, from 1 to 8 DU on the 7-year average, is seen over the industrial area surrounding Beijing. The largest columns are found close to Beijing, where emissions are the largest according to the EDGAR database, and they then decrease westwards.

2. *Norilsk*: located above the polar circle, Norilsk is an industrial area where heavy metals are extracted from sulfide ores. It is also well known for its extremely high levels of pollution (Blacksmith Institutes, 2007), and more particularly for its emissions of $SO_2$ (AMAP, 1998, 2006). The Norilsk smelters are also observed with IASI in Fig. 6, with averaged $SO_2$ columns varying between 1 and 9 DU. A comparison between measurements obtained in this work and those retrieved using an optimal estimation method (Bauduin et al., 2014) is given in Sect. 3.4.1.

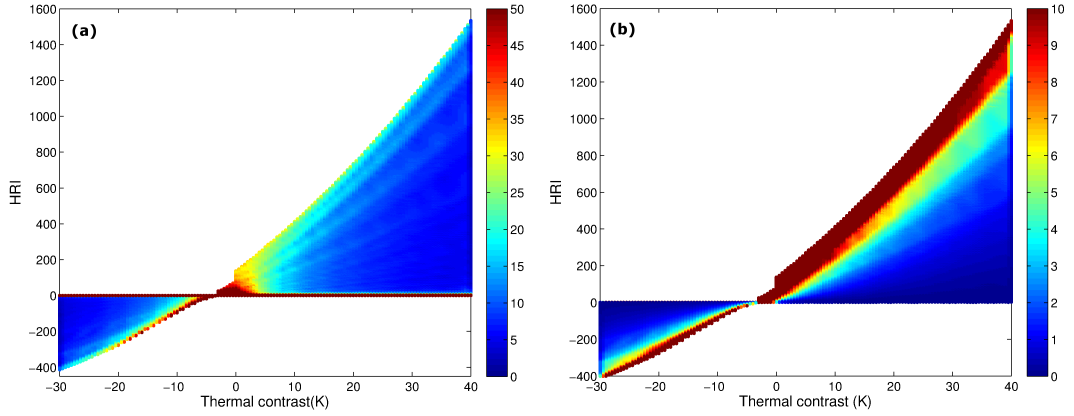



**Figure 5. (a)** Relative errors (%, colour bar) and **(b)** absolute errors (DU, colour bar) as a function of HRI and thermal contrast for a total column of water vapour of $2 \times 10^{20}$ molecules $cm^{-2}$ and for the angle bin of 0–5°.

3. *South Africa*: in Fig. 6, large $SO_2$ columns are observed close to Johannesburg in South Africa, with averaged columns around 3 DU for daytime measurements. Emissions of about $5 \times 10^{-11}$ kg $s^{-1}$ $m^{-2}$ are reported in the EDGAR database in this area, which correspond to power plants of the Mpumalanga Highveld industrial region (Josipovic et al., 2009).

4. *Iran*: several $SO_2$ sources are observed above Iran. Columns of 1 to 4 DU are measured above the smelters of Sar Cheshmeh copper complex (Rastmanesh et al., 2010, 2011). Emissions of oil industries located on the Khark Island (Ardestani and Shafie-Pour, 2009; Fioletov et al., 2013) are also observed, with columns around 1 to 2 DU.

5. *Balkhash*: in Fig. 6, we can see that IASI is able to measure $SO_2$ above the region of copper smelters located in Balkhash, Kazakhstan (Nadirov et al., 2013; Fioletov et al., 2013). Columns around 1 to 2 DU are retrieved.

6. *Mexico and Popocatepetl*: columns reaching more than 10 DU are measured in the region of Mexico City and are regularly detected. These can be attributed to low-altitude plumes released by the Popocatepetl volcano (Varley and Taran, 2003; Grutter et al., 2008) and/or to $SO_2$ emissions of the Tula industrial complex, located north of Mexico City (De Foy et al., 2009). The proximity of these two sources does not however allow us to separate their individual contribution by using IASI observations only.

7. *Kamchatka volcanoes*: $SO_2$ columns of about 2–3 DU are observed above the Kamchatka region. These probably correspond to the activity of different volcanoes located in this region (e.g. Kearney et al. (2008); see also the archive of the Global Volcanism Program: http://volcano.si.edu/).

8. *Nyiragongo*: above the Democratic Republic of Congo, a plume with columns larger than 10 DU is detected. It corresponds to $SO_2$ volcanic degassing from Nyiragongo (Carn et al., 2013) and also probably to emissions of its neighbour, the Nyamuragira (Campion, 2014).

9. *Etna*: in Fig. 6, Mount Etna is covered by $SO_2$, with 0–4 km columns around 6 DU. This volcano is known for its periodic degassing activity and lava-fountaining events (Tamburello et al., 2013; Ganci et al., 2012).

10. *Andes*: a large $SO_2$ plume, with columns around 2–3 DU, is observed in the region of the Andes and can have several origins, which are difficult to distinguish. In the south of Peru, some volcanoes have shown activity in recent years (e.g. Ubinas or Sabancaya; see the archive of the Global Volcanism Program: http://volcano.si.edu/). Copper smelters are located in Ilo (Carn et al., 2007), close to the coast, but are south of the observed plume. $SO_2$ measured above Bolivia and Chile can originate from active volcanoes of the central Andean volcanic zone (Tassi et al., 2011; e.g. the Putana volcano, Stebel et al., 2015). Smelters are also located in this area (Huneeus et al., 2006) and anthropogenic emissions are reported by the EDGAR database. The presence of an artefact in this region, due to the difficulty of representing the emissivity, can however not be totally rejected. Finally, $SO_2$ measured above Argentina, Ecuador and Colombia is mainly emitted by local volcanoes (Global volcanism Program, http://volcano.si.edu/).

11. *Bulgaria*: a narrow plume, with $SO_2$ columns of about 2 DU, is observed in Bulgaria. This corresponds to the Maritsa Iztok Complex of thermal power plants located close to Galabovo and Radnevo (Eisinger and Burrows, 1998; Prodanova et al., 2008).

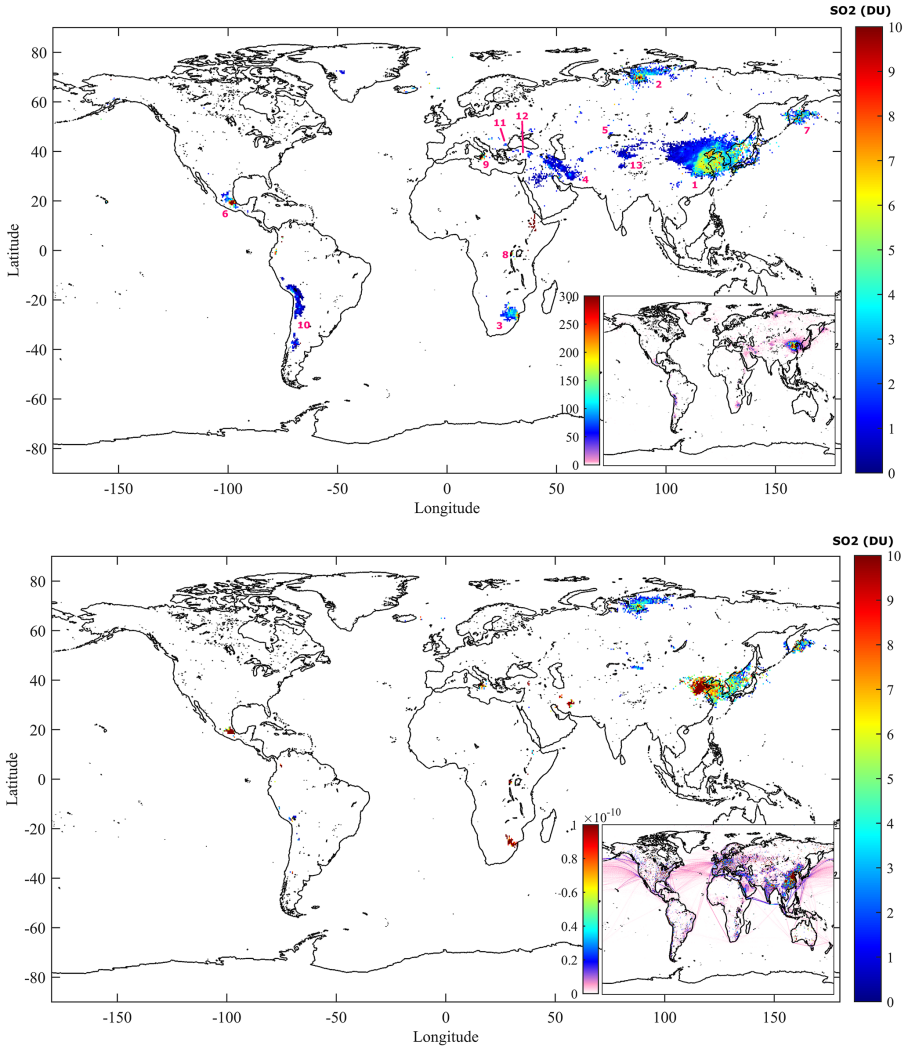



**Figure 6.** Averaged global distribution of near-surface $SO_2$ columns for the period 1 January 2008–30 September 2014. The top panel corresponds to daytime measurements and the bottom panel corresponds to night-time measurements. The bottom-right inset in the daytime map represents the total number of successful measurements (those which pass the error filtering) in each grid box. The bottom-right inset in the night-time map represents the global anthropogenic emissions (kg $s^{-1}$ $m^{-2}$) of $SO_2$ provided by the EDGARv4.2 inventory. Different sources are numbered and discussed in the text. Note that because of the error filtering, the presented global averages are biased high. They can be seen as an average of measurements which are sensitive to near-surface $SO_2$.

12. *Turkey*: in Turkey, lignite-fired power plants are located in different regions and are known to cause air pollution in the vicinity of the complexes (Say, 2006; Vardar and Yumurtaci, 2010). The emissions of these are observed by IASI, with $SO_2$ columns around 2–3 DU.

One unexpected pattern in the daytime distribution is the $SO_2$ plume at the extreme western part of China, corresponding to the Taklamakan Desert (number 13). In this region, the EDGAR inventory only documents a few small sources, but no strong ones are known. While this could be explained by an artefact of the calculated HRI due to sand emissivity, which strongly affects the thermal infrared measurements, it is noteworthy that the issue is not similarly observed above other deserts. For instance, in Fig. 7 we compare the distribution of measured HRI and the total column of $H_2O$ for three desert regions: the Sahara, the centre of Australia and the Taklamakan. We observe that the HRI values are for almost 90 % of the cases below the detection limit of 3 above the Sahara and Australian deserts, whereas 30 % of the measurements over the Taklamakan are associated to a HRI between 3 and 5, and in a few cases even above. It is therefore likely that the measured columns are real, with $SO_2$ being transported from the source regions in east China over the desert or being emitted there by developing gas and oil industries (Lin et al., 2013, http://www.cnpc.com.cn/en/Taklamakan/Taklamakan.shtml). The very high thermal con-

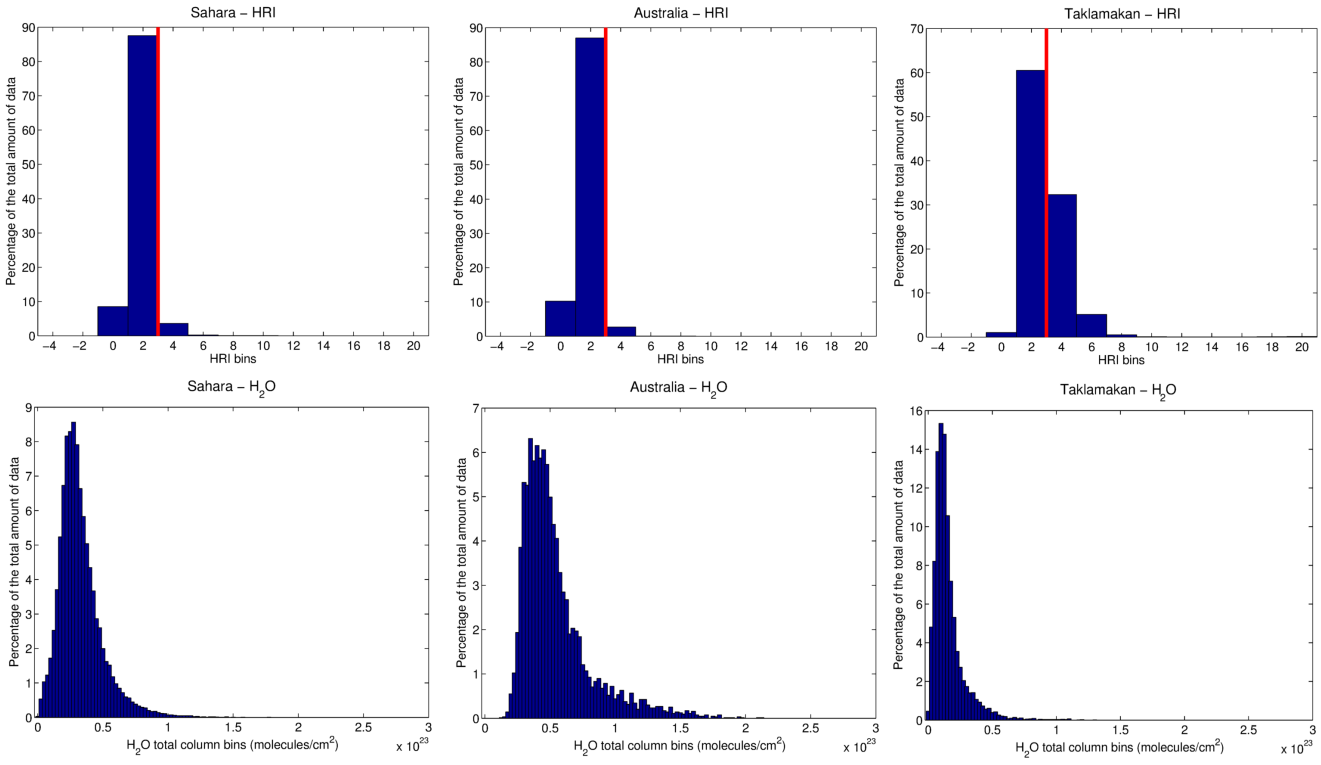



**Figure 7.** Distributions of IASI measurements (expressed in % of the total amount of data considered) as a function of HRI values (top panels) and the total column of $H_2O$ (bottom panels) over the Sahara (left panels), the centre of Australia (middle panels) and Taklamakan (right panels). IASI observations for the period 2011–2014 and located in the areas 18–27° N/6° O–28° E, 29–21° S/121–140° E and 36–40° N/78–86° E have been respectively considered for the Sahara, the centre of Australia and Taklamakan. Only those with less than 20 % cloud coverage and with available L2 temperature and $H_2O$ profiles and surface temperature have been selected. No filter using the error on the retrieved $SO_2$ column has been applied. The red lines in the top panels indicate the detection limit (see Sect. 2.3.2).

trast (up to 20 K) and very low humidity conditions found jointly in that region make it indeed possible to measure such weak columns. However, further investigations are still required to properly assess the source of this detected plume and to exclude possible false attribution due to surface emissivity effects. Finally, the low-altitude parts of the plume released by the Nabro eruption, which followed complex transport patterns (Clarisse et al., 2014), are also seen during day above Ethiopia. Note that $SO_2$ is observed above Iceland and corresponds to the Bardarbunga eruption that started in September 2014 (Schmidt et al., 2015). The different conditions and filters applied on IASI measurements (see the beginning of this section) are responsible for the small area covered by $SO_2$.

It is worth emphasizing that some of the measured points in the 7-year average are only representative of 1 year. For continuous/permanent sources, this indeed depends on the inter-annual variation of thermal contrast and water vapour that limit IASI sensitivity. Moreover, some particular events are typical of some years, like volcanic eruptions. Finally, as mentioned in the beginning of Sect. 3, because of the error filtering, the presented global averages are biased high. It is therefore an average of measurements which are sensitive to near-surface $SO_2$.

Comparison with the EDGAR database has allowed us to identify the observed $SO_2$ plumes. It also points out the sources missed by IASI. Almost year-round low thermal contrasts (January–March and September–December) combined with high humidity in summer (May to September) lead to the absence of eastern US and eastern European sources in Fig. 6. Sources in India and in southeastern Asia are also not observed by IASI. This is likely because of large $H_2O$ amount in the atmosphere in the tropical region, which renders the near-surface atmosphere opaque in the $\nu_3$ band. Note that the joint use of the $\nu_1$ band, less impacted by $H_2O$ absorption, could allow these sources to be detected. The problem of these missing sources is not limited to IASI. OMI $SO_2$ distributions (Figs. 6 and 7 in Theys et al., 2015, and Figs. 1 and 6 in Krotkov et al., 2015) shows the ability of the sounder to measure small sources above India, USA and Europe which are not detected by IASI. These distributions also reveal the absence of some of them, compared to those reported by the EDGAR database: South Eastern Asia (e.g. Thailand), Northern Europe and part of India. These

absences in OMI measurements are possibly caused by unfavourable geophysical conditions (presence of clouds, ...), but this has to be investigated more deeply. However, qualitatively, OMI and IASI global distributions are in good agreement. Both instruments are able to measure large sources such as Northeast China as well as smaller ones, like power plants in Turkey or Bulgaria. The two sounders are also complementary: regions characterized by high humidity and/or low thermal contrasts, undetectable by IASI, can be measured by OMI, whereas IASI better monitors $SO_2$ at high latitudes, especially during the winter, and is not limited to daytime.

When examining Fig. 6, the differences between the $SO_2$ distributions retrieved from IASI measurements during morning (top panel) and evening (bottom panel) overpasses are also striking. In the evening distribution, the plumes are more spatially confined and the columns at the centre of the plumes are generally larger by about a factor of 3. These differences will be discussed in more detail in Sect. 3.3. after the description of the time series below, which provides additional clues about difference.

### 3.2 Time series

In Fig. 8, the 7-year time series (1 January 2008–30 September 2014) above Beijing and the smelters region of Sar Cheshmeh (Iran) are presented as examples. For both areas, daily averages of near-surface $SO_2$ columns, thermal contrast and $H_2O$ total column are shown, separately for the morning (blue) and evening (red) overpasses of IASI. The averages have been calculated within a radius of 125 and 75 km around Beijing and Sar Cheshmeh respectively. As before, only observations with less than 20 % cloud fraction and with available meteorological level 2 have been taken into account and only those satisfying the error filtering are considered.

For Beijing and Sar Cheshmeh, the daily-averaged $SO_2$ columns from the morning overpass vary around 3 DU, with maxima that can reach 15 and 25 DU respectively. The time series is incomplete for Beijing, with successful $SO_2$ retrievals from December to May associated with fairly high thermal contrast (10 K on average but up to 20 K – Fig. 8, middle panels) and low humidity (below $5 \times 10^{22}$ molecules $cm^{-2}$ – Fig. 8, bottom panels). The favourable thermal contrast conditions persist mostly year-round in Beijing but the humidity is too high during the other months to allow us to probe the surface using this IASI scheme. For Sar Cheshmeh, the time series of $SO_2$ columns from the IASI morning overpass is more extensive and this is due to the dryness of the site as compared to Beijing (a factor 2), combined also with persisting high thermal contrast conditions, from 10 K in the colder months to more than 30 K in summer.

It is inferred from Fig. 8 that IASI is mostly not sensitive to surface $SO_2$ above the two sites in the evening due to the drop of thermal contrast close to 0. As already noted in the previous section, the retrieved $SO_2$ columns are larger by at least a factor of 3 in the evening compared to the morning (red vs. blue symbols). This is further investigated in the next section.

### 3.3 Morning–evening differences

To examine the differences in the $SO_2$ distributions from morning and evening overpasses, we focus hereafter on a large area (30–40° N/105–117° E) above China. For this region and for each month in the period 1 January 2008–30 September 2014, we first calculate for morning and evening the fraction of successful $SO_2$ retrievals, i.e. those that pass the prior and posterior filters described in the previous sections and for which the HRI has a correspondence in the LUTs, relative to all the retrievals performed in the considered area. Regarding the last condition, it is important to point out that we found that a number of IASI measurements, mainly associated with negative thermal contrast, were not covered by the LUTs (i.e. their HRI values have no correspondence in the LUTs). The fraction of these measurements is shown in Fig. 9 (left, second panel from top), along with the fraction of successful $SO_2$ retrievals (top panel), as time series. They are compared (as in Fig. 8) to the time evolution of thermal contrast (third panel from top) and water content (bottom panel).

From the top panel we see that the number of successful retrievals during the evening orbit is significantly smaller than during the morning orbit of IASI. In the morning the seasonality is marked, with successful retrievals varying from close to zero in the humid summer months to 20–60 % from January to May. For the evening measurements, the number of successful retrievals stays low year-round and is above 5 % only for 1 or 2 months in spring. The prime rejection criterion for the evening measurements is surprisingly the absence of correspondence, for given angles, thermal contrasts and humidity, between measured and simulated HRI in the LUTs, as obvious from the second panel. This is especially the case in winter (60–80 % of rejected measurements), when thermal contrast is negative and humidity is low.

The fact that such situations are not included in the LUTs comes very likely from a misrepresentation of night-time atmospheric temperature profiles and in particular, temperature inversions with the conditions used to build the LUTs (Table 1). To illustrate this, Fig. 9 (right panel) shows a comparison between the standard temperature profile used and a typical profile retrieved above China (35.81° N/117.81° E) on 29 December 2013. This is a situation for which the thermal contrast is $-5$ K and the water column is $2.42 \times 10^{22}$ molecules $cm^{-2}$, and for which the measured HRI value of $-3.9$ has no correspondence in the LUTs. The simulation of a IASI spectrum with these two temperature profiles, assuming a $SO_2$ column of 4.35 DU, results in totally different values of the HRI, $+1.2$ for the US Stan-

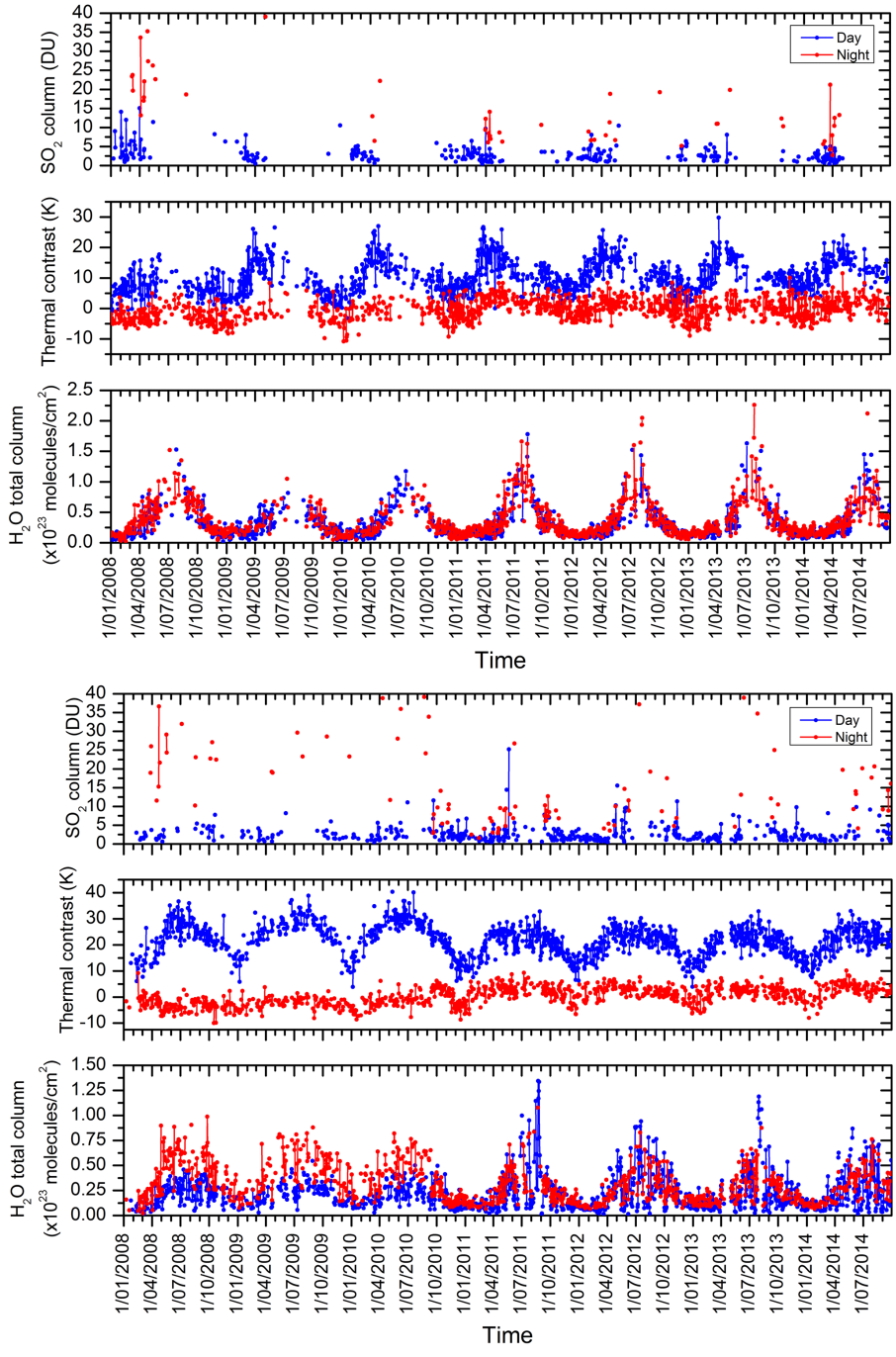



**Figure 8.** Daily averages of near-surface $SO_2$ (DU), thermal contrast (K) and $H_2O$ total column (molecules $cm^{-2}$) above Beijing (top panels) and Sar Cheshmeh (bottom panels). Averages have been calculated within a radius of 125 and 75 km of Beijing and Sar Cheshmeh respectively. Daytime measurements are indicated in blue and night-time measurements are indicated in red.

dard temperature profile and −4.1 for the retrieved temperature profile. These results pinpoint a limitation of the current LUTs for slightly negative thermal contrast (it is not observed for large temperature inversions), which is a range where the competition between absorption and emission contributions to the HRI vary drastically. More work will be needed to avoid this shortcoming of the method in the future, either by including more temperature profiles in the calculation of the LUTs or by using alternative approaches to better account for the variety of real situations encountered. Note that errors on the thermal contrast and on the assumed $SO_2$ vertical profile also affect the HRI and, as a consequence,

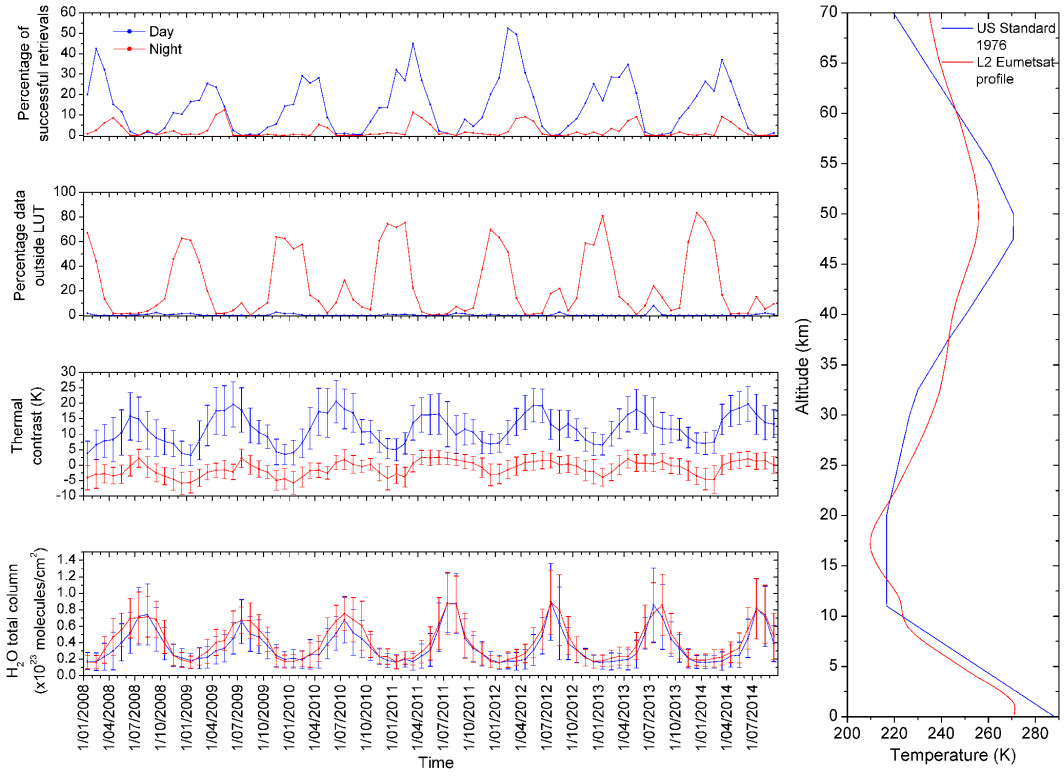



**Figure 9.** Left panels (from top to bottom): (1) monthly percentage of successful retrievals (see text), (2) monthly percentage of measurements outside the LUT, (3) monthly averages of thermal contrast (K) with associated standard deviations, (4) monthly averages of the total column of $H_2O$ (molecules $cm^{-2}$) with associated standard deviations. Daytime measurements correspond to blue and night-time measurements to red. Right panel: temperature vertical profiles of the US Standard 1976 model (blue) and given by the EUMETSAT L2 product (red) for the IASI spectrum recorded above China at 35.81° N/117.81° E on 29 December 2013.

the retrieved $SO_2$ column. They could be partly responsible for the observed non-correspondence between measured HRI and the LUTs.

The small number of successful retrievals in the evening measurements, combined with the generally lower sensitivity of IASI in this period of the day, is likely responsible in part for the factor 2–3 difference observed in the $SO_2$ columns between morning and evening measurements. Indeed, as only the retrieved $SO_2$ columns with small errors are kept, and as in the evening these are mainly those with large columns, the averages are biased high. The effect also exists for the morning measurements but is less pronounced because of the better sensitivity to smaller columns with the atmospheric conditions – particularly thermal contrast – encountered. Another possible cause for the larger concentrations is photochemistry. During the day, the photochemistry is more active and the concentrations of oxidants such as OH, $H_2O_2$ and $O_3$ are high, creating an important sink for $SO_2$, which disappears at night, favourizing higher concentrations. Such a diurnal cycle of $SO_2$ has been observed previously in China (Wang, 2002; Wang et al., 2014) and in other regions of the world (Khemani et al., 1987; Psiloglou et al., 2013), but in others, noontime $SO_2$ peaks have also been observed (e.g. Lin et al., 2012; Xu et al., 2014), possibly as a result of other meteorological/dynamical effects (Xu et al., 2014).

### 3.4 Product evaluation

#### 3.4.1 Comparisons with an optimal estimation retrieval scheme

As already mentioned in Sect. 3.1, Norilsk is an industrial area located in Siberia that emits large quantities of $SO_2$. Recently, taking the advantages of the large temperature inversions that develop in winter in the region, we have monitored $SO_2$ in this area for the first time with the IASI sounder over several years (Bauduin et al., 2014), by using a method relying on the iterative optimal estimation (Rodgers, 2000) and exploiting a generalized spectral noise covariance matrix (see also Carboni et al., 2012). As a first assessment of the low-altitude $SO_2$ column product developed in this work, we compare the resulting 0–4 km $SO_2$ columns with the 0–5 km columns retrieved by Bauduin et al. (2014). The results are presented in Fig. 10. For the comparison, we consider observations located within a 150 km radius around the city of Norilsk. Only measurements of Bauduin et al. (2014) with less

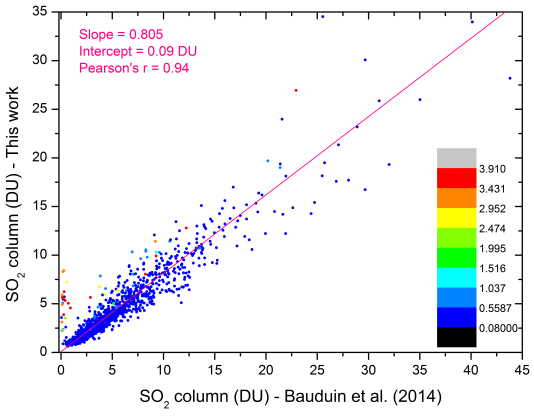



**Figure 10.** Comparison between $SO_2$ columns retrieved above the industrial area of Norilsk using the retrieval method developed in this work and the 0–5 km $SO_2$ columns retrieved in Bauduin et al. (2014). Measurements located within a radius of 150 km centred in Norilsk with less than 25 % cloud coverage and retrieved with relative errors smaller than 25 % and absolute errors smaller than 10 DU have been taken into account. Furthermore, only measurements with a $H_2O$ amount at 350 m lower than 4 g kg$^{-1}$ and with thermal contrast larger than 5 K in absolute value have been considered (see detailed explanations in the text). The pink line corresponds to the linear regression (reduced major axis) calculated between the two sets of data. The colour bar represents the humidity at 350 m expressed in g kg$^{-1}$.

than 25 % cloud fraction, with a thermal contrast larger than 5 K in absolute value and with a humidity below 4 g kg$^{-1}$ at 350 m above ground have been selected (this altitude corresponds to the average height of the temperature inversions). These last conditions ensure that near-surface $SO_2$ is indeed probed, as explained in Bauduin et al. (2014) and also well visualized in their Fig. 3. Finally, we only consider the $SO_2$ columns retrieved with the method described in this work satisfying the error criteria. The entire period 2008–2013 is analysed, resulting in a total of 1233 pairs of columns to compare. The comparison between the two sets of $SO_2$ columns is shown in Fig. 10. A linear regression is also shown between the two coincident sets of data using the reduced major axis method (Smith et al., 2009) to account for the fact that both data sets come with errors. The agreement between the columns is very good, characterized by a correlation coefficient of 0.94. The intercept, which is close to zero, and the slope of 0.80 indicate that the $SO_2$ columns retrieved using the LUT tend to be 20 % smaller than those retrieved with the iterative method of Bauduin et al. (2014). This difference is partly due to the difference in columns (0–4 km with the newly developed method against 0–5 km in Bauduin et al., 2014) and to the difference in the profile used to build the LUTs with the a priori profile used in the iterative method. The use of the constant temperature profile for the LUTs can also cause this difference.

Finally, it is worth emphasizing in Fig. 10 the measurements for which the LUTs provide a column above 2.5–3 DU and the optimal estimation retrieval of a column close to 0 corresponding to the a priori column. As obvious from the colour scale, these retrievals are all associated with a relatively high humidity of 3 g kg$^{-1}$. These measurements have a significant HRI around 5, indicating small signal strength, which is probably the reason of the difference observed between the two methods.

### 3.4.2 Comparisons with OMI-derived $SO_2$ columns

OMI is an imaging spectrograph that operates in a nadir-viewing mode in the ultraviolet–visible spectral range 270–500 nm, and was launched in 2004 on the EOS-Aura NASA platform (details are given in Levelt et al., 2006). We perform a comparison of the retrieved 0–4 km $SO_2$ column from IASI and those retrieved from OMI using the algorithm of Theys et al. (2015) for anthropogenic $SO_2$. For the IASI column, the same filters on cloud fraction and errors as described in Sects. 3.1 and 3.2 are applied. For the OMI columns, only those retrieved in the spectral range 312–326 nm from measurements not affected too much by the row anomaly, with solar zenith angles smaller than 65° and less than 30 % cloud fraction are used (see Theys et al. (2015) for details). The comparison is performed on monthly averages for the period 2010–2013 and for an area corresponding to a radius of 125 km around Beijing. Figure 11 shows the comparison in terms of (top panel) a time series of the monthly averaged columns of IASI (blue) and OMI (red squares for the standard retrieval and green triangles for the retrieval using a different air mass factor – AMF), and in terms of regional maps (2010–2013) above China (bottom panels). From Fig. 11, it can be seen that the IASI columns are on average a factor of 2.5 larger. The mean relative difference between the monthly averages of the two instruments is −135 % (OMI-IASI/OMI). This difference has several origins. Firstly, monthly means calculated from IASI are probably overestimated by the fact that only the columns with low errors are kept, which favours the higher values of the columns. Secondly, it is likely that OMI $SO_2$ columns are underestimated. This has already been observed by Theys et al. (2015) above Xianghe (China), in the comparison with MAX-DOAS measurements (Wang et al., 2014) and explained by the inappropriate AMF used to convert the OMI-derived $SO_2$ slant column densities in vertical column densities. In their study, Theys et al. showed that the use of better AMF significantly improves the agreement between MAX-DOAS and OMI observations. For the sake of illustration, we also show in Fig. 11 the $SO_2$ vertical column densities from OMI retrieved using the method of Theys et al. (2015), but with a constant AMF of 0.4, which is the one used in the operational OMI PBL $SO_2$ product (Krotkov et al., 2008). With this correction, the agreement between the two instruments is improved; the mean relative difference becomes −65 %. Dis-

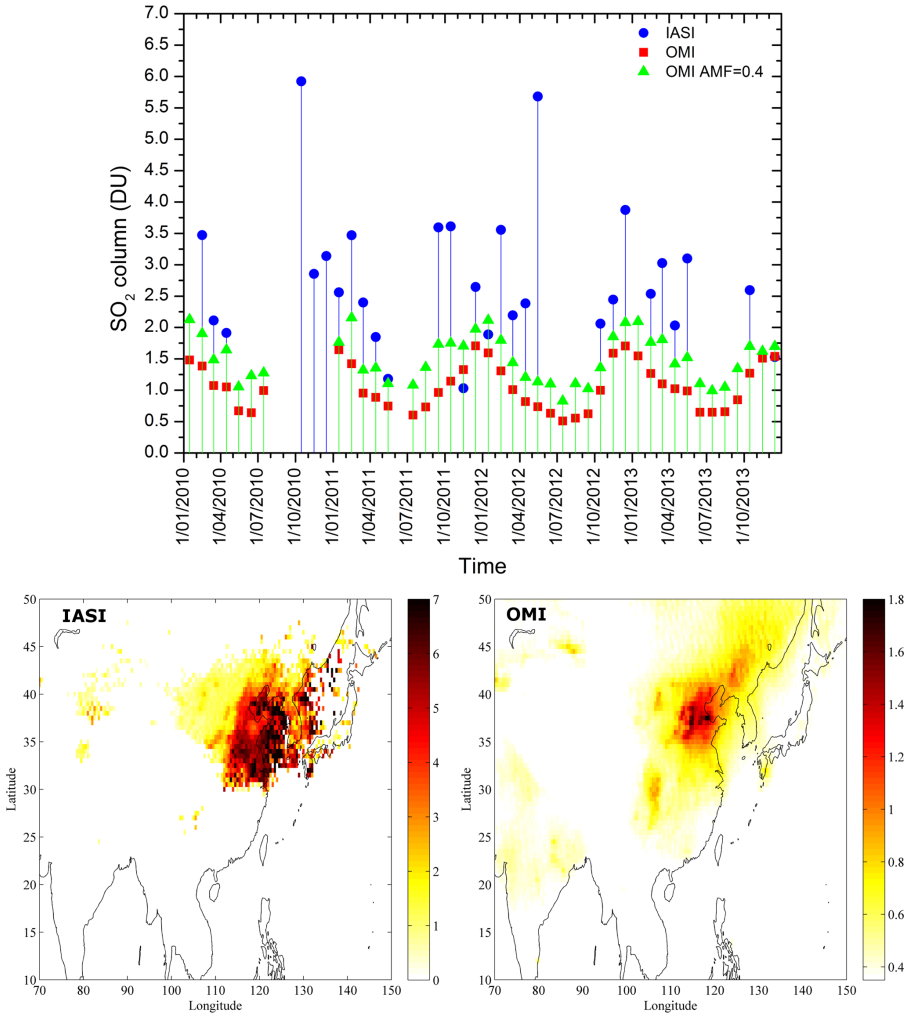



**Figure 11.** Top panel: monthly mean $SO_2$ columns (DU) retrieved for the period 2010–2013 above Beijing within a 125 km radius from IASI (blue) and OMI (red) observations. Green triangles correspond to OMI measurements for which an AMF of 0.4 has been used to calculate vertical $SO_2$ columns. Details are given in the text. Bottom panels: spatial distributions of $SO_2$ (DU, different colour scales) above China for the period 2010–2013 from IASI observations (left panel) and from OMI observations (right panel, without AMF changes). $SO_2$ columns have been averaged on a $0.5° \times 0.5°$ grid.

crepancies are within the range of what we can expect given the difference in the overpass times of the two satellites and given the high bias introduced by averaging only the IASI observations with a low relative uncertainty. Note also that the difference between the vertical sensitivity profiles of the two instruments can also contribute to observed differences.

Finally, we have calculated the correlation coefficient between IASI and OMI measurements. It is very low for both OMI data sets, $-0.03$ and 0.15 respectively for the varying AMF and AMF $= 0.4$. These low values are mainly caused by one outlier on May 2012, where IASI has a large $SO_2$ column of 5.7 DU, which corresponds, however, to very few measurements (three). These coefficients significantly improve when this outlier is removed; they become respectively 0.23 and 0.54.

## 4 Conclusions

In this work, we have presented a method for retrieving $SO_2$ in the low troposphere from IASI at a global scale. The method follows two steps, both relying on the calculation of hyperspectral range indexes (HRIs), which represent the strength of $SO_2$ spectral signal in IASI measurements. In the first step, the altitude of $SO_2$ plumes is retrieved and all plumes with altitude above 4 km (from ground), likely from volcanic origin, are rejected. For the remaining low-altitude plumes, HRI values are converted into 0–4 km (ground to 4 km above it) $SO_2$ columns using look-up tables. The construction of the LUTs is a key part of the method; it is done from forward model simulations taking the thermal contrast, the total column of $H_2O$ and the zenith angle into account.

Tables of errors have been associated with each LUT, allowing the error characterization of each retrieved $SO_2$ column and the posterior selection of the retrieved $SO_2$ columns for which IASI is sensitive enough. We have estimated for day and night, respectively, that 10 and 7 % of the total IASI observations are taken in the favourable conditions required to measure near-surface $SO_2$. Also, from calculated Jacobians, we have shown that IASI's sensitivity to $SO_2$ increases with altitude, but in the case of favourable conditions of thermal contrast and water vapour, the instrument is sensitive to $SO_2$ down to the surface.

The method has been applied to IASI data from 1 January 2008 to 30 September 2014 to provide global distributions and time series for the 0–4 km column. The average global distribution reveals the large known anthropogenic $SO_2$ sources, such as the Norilsk and Sar Cheshmeh smelters, the power plants in South Africa and the large industrial region in Northeast China. Smaller sources, e.g. power plants in Bulgaria, are also measured. In addition to this, low-altitude plumes from degassing volcanoes are also detected. Non-negligible $SO_2$ columns have been retrieved above the Taklamakan Desert and this was explained by enhanced sensitivity of IASI in this region characterized by extremely low humidity and high thermal contrast; the source of the $SO_2$ remains to be assessed. Similarly, the generally favourable conditions occurring in Sar Cheshmeh (Iran) have allowed us to acquire the daily time evolution of the $SO_2$ column almost completely over the entire 7 years. This was not the case for the Beijing area that we selected as another example region, where we show that IASI sensitivity has a strong seasonal cycle such that the $SO_2$ columns can only be retrieved with small errors for the period December–May, corresponding to the driest months. The retrieved 0–4 km $SO_2$ columns from IASI have been compared to those of OMI on a monthly averaged basis. A high bias of 135 % has been revealed, decreasing to 65 %, depending on the choice of the AMF used in the OMI retrievals. The high bias is likely linked to an overestimation of IASI averages due to the error filtering applied on the data. More comparisons and validation work are needed to investigate the observed differences between the two instruments more deeply. The two instruments are nevertheless complementary; regions characterized by high humidity and/or low thermal contrasts can be measured by OMI, whereas IASI better monitors $SO_2$ at high latitudes, especially during the winter, and is not limited to daytime. Another assessment of the retrieval method was provided by comparing the retrieved $SO_2$ columns from IASI with the LUT-based approach to those retrieved from the same measurements with an iterative optimal estimation scheme; a good correspondence was found between the two column data sets (correlation coefficient of 0.94, with the LUT lower by 20 %) considering the different assumptions and input profiles used in the two methods. This excellent agreement shows how well the new method is able to retrieve near-surface $SO_2$. It has the advantage of being very fast; iterations and the retrieval of interfering parameters are not needed. In contrast to the optimal estimation method, it is, however, not able to provide a full retrieval characterization of the retrieved columns/profiles, notably in terms of vertical sensitivity.

Finally, striking differences between morning and evening $SO_2$ distributions retrieved from IASI were shown, with the $SO_2$ columns retrieved in the evening being more spatially confined and larger than those in the morning by a factor of 2–3. While changes in photochemistry and a larger high-bias in the night averages could explain part of this effect, we have shown that it is most probably due to a shortcoming of the LUT, which relies on a single temperature profile and is not able to deal well with temperature inversions, which develop in the evening and in winter. Further developments will be needed to correct for this and to allow a better representativeness of the variety of temperature, $SO_2$ and $H_2O$ profiles occurring globally. The use of both $\nu_3$ and $\nu_1$ bands can also be envisaged to reduce the impact of $H_2O$ absorption and to increase the IASI sensitivity to surface $SO_2$. Despite this, given the preliminary comparisons, the results obtained with this new method are however very encouraging, especially for daytime, and constitute the first successful attempt to retrieve near-surface $SO_2$ globally with the IASI thermal infrared sensor. The continuation of this program is ensured by the upcoming launch of MetOp-C (2018) and in the longer term, by the IASI-NG mission onboard MetOp-SG (Crevoisier et al., 2014).

*Acknowledgements.* IASI has been developed and built under the responsibility of the Centre National d'Etudes Spatiales (CNES, France). It is flown on board the MetOp satellites as part of the EUMETSAT Polar System. The IASI L1 data are received through the EUMETCast near-real-time data distribution service. The research in Belgium was funded by the F.R.S.-FNRS, the Belgian State Federal Office for Scientific, Technical, and Cultural Affairs, and the European Space Agency (ESA-Prodex arrangements). Financial support by the "Actions de Recherche Concertée" (Communauté Française de Belgique) is also acknowledged. S. Bauduin, L. Clarisse and P.-F. Coheur are, respectively, Research Fellow, Research Associate and Senior Research Associate with F.R.S.-FNRS. C. Clerbaux is grateful to the CNES for scientific collaboration and financial support. We would like to thank D. Hurtmans for the development of the Atmosphit software. We also acknowledge the Ether/ECCAD database for the archiving and the distribution of the EDGAR v4.2 emission inventory.

Edited by: H. Worden

## References


Ali-Khodja, H. and Kebabi, B.: Assessment of wet and dry deposition of $SO_2$ attributable to a sulfuric acid plant at Annaba, Algeria, Environ. Int., 24, 799–807, doi:10.1016/s0160-4120(98)00059-2, 1998.

AMAP – Arctic Monitoring and Assessment Programme: Acidifying Pollutants, Arctic Haze, and Acidification in the Arctic, Chap. 9, Arctic Monitoring and Assessment Programme (AMAP), Oslo, 621–659, 1998.

AMAP – Arctic Monitoring and Assessment Programme: Acidifying Pollutants, Arctic Haze, and Acidification in the Arctic, Arctic Monitoring and Assessment Programme (AMAP), Oslo, 2006.

Anderson, G., Clough, S., Kneizys, F., Chetwynd, J., and Shettle, E. P.: AFGL Atmospheric Constituent Profiles (0–120 km), AFGL-TR-86-0110, Environmental Research Papers, 954, ADA175173, 1986.

Andres, R. J. and Kasgnoc, A. D.: A time-averaged inventory of subaerial volcanic sulfur emissions, J. Geophys. Res., 103, 25251-25261, doi:10.1029/98jd02091, 1998.

Ardestani, M. and Shafie-Pour, M.: Environmentally compatible energy resource production-consumption pattern (case study: Iran), Environ. Dev. Sustain., 11, 277–291, doi:10.1007/s10668-007-9110-7, 2009.

August, T., Klaes, D., Schlüssel, P., Hultberg, T., Crapeau, M., Arriaga, A., O'Carroll, A., Coppens, D., Munro, R., and Calbet, X.: IASI on Metop-A: Operational Level 2 retrievals after five years in orbit, J. Quant. Spectrosc. Ra., 113, 1340–1371, doi:10.1016/j.jqsrt.2012.02.028, 2012.

Bauduin, S., Clarisse, L., Clerbaux, C., Hurtmans, D., and Coheur, P.-F.: IASI observations of sulfur dioxide ($SO_2$) in the boundary layer of Norilsk, J. Geophys. Res.-Atmos., 119, 4253–4263, doi:10.1002/2013JD021405, 2014.

Blacksmith Institutes: The World's Worst Polluted Places – The Top Ten of The Dirty Thirty, New York, 2007.

Boynard, A.and Clerbaux, C., Clarisse, L., Safieddine, S., Pommier, M., Van Damme, M., Bauduin, S., Oudot, C., Hadji-Lazaro, J., Hurtmans, D., and Coheur, P.-F.: First space measurements of simultaneous pollutants in the boundary layer from IASI: a case study in the North China Plain, Geophys. Res. Lett., 41, 645–651, doi:10.1002/2013GL058333, 2014.

Campion, R.: New lava lake at Nyamuragira volcano revealed by combined ASTER and OMI $SO_2$ measurements, Geophys. Res. Lett., 41, 7485–7492, doi:10.1002/2014gl061808, 2014.

Carboni, E., Grainger, R., Walker, J., Dudhia, A., and Siddans, R.: A new scheme for sulphur dioxide retrieval from IASI measurements: application to the Eyjafjallajökull eruption of April and May 2010, Atmos. Chem. Phys., 12, 11861–11897, doi:10.5194/acp-12-11417-2012, 2012.

Carn, S. A., Krueger, A. J., Bluth, G. J. S., Schaefer, S. J., Krotkov, N. A., Watson, I. M., and Datta, S.: Volcanic eruption detection by the Total Ozone Mapping Spectrometer (TOMS) instruments: a 22-year record of sulphur dioxide and ash emissions, Geol. Soc. Lond. Spec. Publ., 213, 177–202, doi:10.1144/gsl.sp.2003.213.01.11, 2003.

Carn, S. A., Strow, L. L., De Souza-Machado, S., Edmonds, Y., Hannon, S.: Quantifying tropospheric volcanic emissions with AIRS: The 2002 eruption of Mt. Etna (Italy), Geophys. Res. Lett., 32, L02301, doi:10.1029/2004GL021034, 2005.

Carn, S. A., Krueger, A. J., Krotkov, N. A., Yang, K., and Levelt, P. F.: Sulfur dioxide emissions from Peruvian copper smelters detected by the Ozone Monitoring Instrument, Geophys. Res. Lett., 34, L09801, doi:10.1029/2006GL029020, 2007.

Carn, S. A., Krotkov, N. A., Yang, K., and Krueger, A. J.: Measuring global volcanic degassing with the Ozone Monitoring Instrument (OMI), Geol. Soc. Lond. Spec. Publ., 380, 229–257, doi:10.1144/sp380.12, 2013.

Clarisse, L., Coheur, P.-F., Prata, A. J., Hurtmans, D., Razavi, A., Phulpin, T., Hadji-Lazaro, J., and Clerbaux, C.: Tracking and quantifying volcanic $SO_2$ with IASI, the September 2007 eruption at Jebel at Tair, Atmos. Chem. Phys., 8, 7723–7734, doi:10.5194/acp-8-7723-2008, 2008.

Clarisse, L., Shephard, M. W., Dentener, F., Hurtmans, D., Cady-Pereira, K., Karagulian, F., Van Damme, M., Clerbaux, C., and Coheur, P.-F.: Satellite monitoring of ammonia: A case study of the San Joaquin Valley, J. Geophys. Res., 115, doi:10.1029/2009JD013291, 2010.

Clarisse, L., Coheur, P.-F., Prata, F., Hadji-Lazaro, J., Hurtmans, D., and Clerbaux, C.: A unified approach to infrared aerosol remote sensing and type specification, Atmos. Chem. Phys., 13, 2195–2221, doi:10.5194/acp-13-2195-2013, 2013.

Clarisse, L., Coheur, P.-F., Theys, N., Hurtmans, D., and Clerbaux, C.: The 2011 Nabro eruption, a $SO_2$ plume height analysis using IASI measurements, Atmos. Chem. Phys., 14, 3095–3111, doi:10.5194/acp-14-3095-2014, 2014.

Clerbaux, C., Coheur, P.-F., Clarisse, L., Hadji-Lazaro, J., Hurtmans, D., Turquety, S., Bowman, K., Worden, H., and Carn, S.: Measurments of $SO_2$ profiles in volcanic plumes from the NASA Tropospheric Emission Spectrometer (TES), Geophys. Res. Lett., 35, L22807, doi:10.1029/2008GL035566, 2008.

Clerbaux, C., Boynard, A., Clarisse, L., George, M., Hadji-Lazaro, J., Herbin, H., Hurtmans, D., Pommier, M., Razavi, A., Turquety, S., Wespes, C., and Coheur, P.-F.: Monitoring of atmospheric composition using the thermal infrared IASI/MetOp sounder, Atmos. Chem. Phys., 9, 6041–6054, doi:10.5194/acp-9-6041-2009, 2009.

Coheur, P.-F., Barret, B., Turquety, S., Hurtmans, D., Hadji-Lazaro, J., and Clerbaux, C.: Retrieval and characterization of ozone vertical profiles from a thermal infrared nadir sounder, J. Geophys. Res., 110, D24303, doi:10.1029/2005JD005845, 2005.

Crevoisier, C., Clerbaux, C., Guidard, V., Phulpin, T., Armante, R., Barret, B., Camy-Peyret, C., Chaboureau, J.-P., Coheur, P.-F., Crépeau, L., Dufour, G., Labonnote, L., Lavanant, L., Hadji-Lazaro, J., Herbin, H., Jacquinet-Husson, N., Payan, S., Péquignot, E., Pierangelo, C., Sellitto, P., and Stubenrauch, C.: Towards IASI-New Generation (IASI-NG): impact of improved spectral resolution and radiometric noise on the retrieval of thermodynamic, chemistry and climate variables, Atmos. Meas. Tech., 7, 4367–4385, doi:10.5194/amt-7-4367-2014, 2014.

De Foy, B., Krotkov, N. A., Bei, N., Herndon, S. C., Huey, L. G., Martínez, A.-P., Ruiz-Suárez, L. G., Wood, E. C., Zavala, M., and Molina, L. T.: Hit from both sides: tracking industrial and volcanic plumes in Mexico City with surface measurements and OMI $SO_2$ retrievals during the MILAGRO field campaign, Atmos. Chem. Phys., 9, 9599–9617, doi:10.5194/acp-9-9599-2009, 2009.

EDGAR – Emission Database for Global Atmospheric Research: European Commission, Joint Research Cen-

tre (JRC)/Netherlands Environmental Assessment Agency (PBL), Emission Database for Global Atmospheric Research (EDGAR), release version 4.2, http://edgar.jrc.ec.europa.eu (last access: 10 August 2015), 2011.

Eisinger, M. and Burrows, J. P.: Tropospheric Sulfur Dioxide observed by the ERS-2 GOME Instrument, Geophys. Res. Lett., 25, 4177–4180, 1998.

Emmons, L. K., Walters, S., Hess, P. G., Lamarque, J.-F., Pfister, G. G., Fillmore, D., Granier, C., Guenther, A., Kinnison, D., Laepple, T., Orlando, J., Tie, X., Tyndall, G., Wiedinmyer, C., Baughcum, S. L., and Kloster, S.: Description and evaluation of the Model for Ozone and Related chemical Tracers, version 4 (MOZART-4), Geosci. Model Dev., 3, 43–67, doi:10.5194/gmd-3-43-2010, 2010.

Fioletov, V. E., McLinden, C. A., Krotkov, N., Moran, M. D., and Yang, K.: Estimation of $SO_2$ emissions using OMI retrievals, Geophys. Res. Lett., 38, L21811, doi:10.1029/2011GL049402, 2011.

Fioletov, V. E., McLinden, C. A., Krotkov, N., Yang, K., Loyola, D. G., Valks, P., Theys, N., Van Roozendael, M., Nowlan, C. R., Chance, K., Liu, X., Lee, C., and Martin, R. V.: Application of OMI, SCIAMACHY, and GOME-2 satellite $SO_2$ retrievals for detection of large emission sources, J. Geophys. Res.-Atmos., 118, 11399–11418, doi:10.1002/jgrd.50826, 2013.

Fioletov, V. E., McLinden, C. A., Krotkov, N., and Li, C.: Lifetimes and emissions of $SO_2$ from point sources estimated from OMI, Geophys. Res. Lett., 42, 1969–1976, doi:10.1002/2015gl063148, 2015.

Ganci, G., Harris, A. J. L., Del Negro, C., Guehenneux, Y., Cappello, A., Labazuy, P., Calvari, S., and Gouhier, M.: A year of lava fountaining at Etna: Volumes from SEVIRI, Geophys. Res. Lett., 39, L06305, doi:10.1029/2012gl051026, 2012.

Grutter, M., Basaldud, R., Rivera, C., Harig, R., Junkerman, W., Caetano, E., and Delgado-Granados, H.: $SO_2$ emissions from Popocatépetl volcano: emission rates and plume imaging using optical remote sensing techniques, Atmos. Chem. Phys., 8, 6655–6663, doi:10.5194/acp-8-6655-2008, 2008.

Halmer, M., Schmincke, H.-U., and Graf, H.-F.: The annual volcanic gas input into the atmosphere, in particular into the stratosphere: a global data set for the past 100 years, J. Volcanol. Geoth. Res., 115, 511–528, doi:10.1016/s0377-0273(01)00318-3, 2002.

Hilton, F., Armante, R., August, T., Barnet, C., Bouchard, A., Camy-Peyret, C., Capelle, V., Clarisse, L., Clerbaux, C., Coheur, P.-F., Collard, A., Crevoisier, C., Dufour, G., Edwards, D., Faijan, F., Fourrié, N., Gambacorta, A., Goldberg, M., Guidard, V., Hurtmans, D., Illingworth, S., Jacquinet-Husson, N., Kerzenmacher, T., Klaes, D., Lavanant, L., Masiello, G., Matricardi, M., McNally, A., Newman, S., Pavelin, E., Payan, S., Péquignot, E., Peyridieu, S., Phulpin, T., Remedios, J., Schlüssel, P., Serio, C., Strow, L., Stubenrauch, C., Taylor, J., Tobin, D., Wolf, W., and Zhou, D.: Hyperspectral Earth observation from IASI – Five Years of Accomplishments, B. Am. Meteorol. Soc., 93, 347–370, doi:10.1175/BAMS-D-11-00027.1, 2012.

Huneeus, N., Gallardo, L., and Rutllant, J. A.: Offshore transport episodes of anthropogenic sulfur in northern Chile: Potential impact on the stratocumulus cloud deck, Geophys. Res. Lett., 33, L19819, doi:10.1029/2006gl026921, 2006.

Josipovic, M., Annegarn, H. J., Kneen, M. A., Pienaar, J. J., and Piketh, S. J.: Concentrations, distributions and critical level exceedance assessment of $SO_2$, $NO_2$ and $O_3$ in South Africa, Environ. Monit. Assess., 171, 181–196, doi:10.1007/s10661-009-1270-5, 2009.

Kearney, C. S., Dean, K., Realmuto, V. J., Watson, I. M., Dehn, J., and Prata, F.: Observations of $SO_2$ production and transport from Bezymianny volcano, Kamchatka using the MODerate resolution Infrared Spectroradiometer (MODIS), Int. J. Remote Sens., 29, 6647–6665, doi:10.1080/01431160802168392, 2008.

Khemani, L. T., Momin, G. A., and Singh, G.: Variations in trace gas concentrations in different environments in India, Pure Appl. Geophys., 125, 167–181, doi:10.1007/bf00878620, 1987.

Krotkov, N. A., Carn, S. A., Krueger, A. J., Bhartia, P. K., and Yang, K.: Band Residual Difference Algorithm for Retrieval of $SO_2$ From the Aura Ozone Monitoring Instrument (OMI), IEEE T. Geosci. Remote, 44, 1259–1266, doi:10.1109/TGRS.2005.861932, 2006.

Krotkov, N. A., McClure, B., Dickerson, R. R., Carn, S. A., Li, C., Bhartia, P. K., Yang, K., Krueger, A. J., Li, Z., Levelt, P. F., Chen, H., Wang, P., and Lu, D.: Validation of $SO_2$ retrievals from the Ozone Monitoring Instrument over NE China, J. Geophys. Res., 113, D16S40, doi:10.1029/2007JD008818, 2008.

Krotkov, N. A., McLinden, C. A., Li, C., Lamsal, L. N., Celarier, E. A., Marchenko, S. V., Swartz, W. H., Bucsela, E. J., Joiner, J., Duncan, B. N., Boersma, K. F., Veefkind, J. P., Levelt, P. F., Fioletov, V. E., Dickerson, R. R., He, H., Lu, Z., and Streets, D. G.: Aura OMI observations of regional $SO_2$ and $NO_2$ pollution changes from 2005 to 2014, Atmos. Chem. Phys. Discuss., 15, 26555-26607, doi:10.5194/acpd-15-26555-2015, 2015.

Krueger, A. J.: Sighting of El Chichon Sulfur Dioxide Clouds with the Nimbus 7 Total Ozone Mapping Spectrometer, Science, 220, 1377–1379, doi:10.1126/science.220.4604.1377, 1983.

Lee, C., Richter, A., Weber, M., and Burrows, J. P.: $SO_2$ Retrieval from SCIAMACHY using the Weighting Function DOAS (WF-DOAS) technique: comparison with Standard DOAS retrieval, Atmos. Chem. Phys., 8, 6137–6145, doi:10.5194/acp-8-6137-2008, 2008.

Lee, C., Martin, R. V., Van Donkelaar, A., Lee, H., Dickerson, R. R., Hains, J. C., Krotkov, N., Richter, A., Vinnikov, K., and Schwab, J. J.: $SO_2$ emissions and lifetimes: Estimates from inverse modeling using in situ and global, space-based (SCIAMACHY and OMI) observations, J. Geophys. Res., 116, D06304, doi:10.1029/2010JD014758, 2011.

Levelt, P., van den Oord, G., Dobber, M., Malkki, A., Visser, H., de Vries, J., Stammes, P., Lundell, J., and Saari, H.: The ozone monitoring instrument, IEEE T. Geosci. Remote, 44, 1093–1101, doi:10.1109/tgrs.2006.872333, 2006.

Lin, W., Xu, X., Ma, Z., Zhao, H., Liu, X., and Wang, Y.: Characteristics and recent trends of sulfur dioxide at urban, rural, and background sites in North China: Effectiveness of control measures, J. Environ. Sci., 24, 34–49, doi:10.1016/S1001-0742(11)60727-4, 2012.

Lin, W., Xu, X., Yu, X., Zhang, X., and Huang, J.: Observed levels and trends of gaseous $SO_2$ and $HNO_3$ at Mt. Waliguan, China: Results from 1997 to 2009, J. Environ. Sci., 25, 726–734, doi:10.1016/s1001-0742(12)60143-0, 2013.

Lu, Z., Streets, D. G., Zhang, Q., Wang, S., Carmichael, G. R., Cheng, Y. F., Wei, C., Chin, M., Diehl, T., and Tan, Q.: Sulfur

dioxide emissions in China and sulfur trends in East Asia since 2000, Atmos. Chem. Phys., 10, 6311–6331, doi:10.5194/acp-10-6311-2010, 2010.

McLinden, C. A., Fioletov, V., Boersma, K. F., Krotkov, N., Sioris, C. E., Veefkind, J. P., and Yang, K.: Air quality over the Canadian oil sands: A first assessment using satellite observations, Geophys. Res. Lett., 39, L04804, doi:10.1029/2011GL050273, 2012.

McLinden, C. A., Fioletov, V., Boersma, K. F., Kharol, S. K., Krotkov, N., Lamsal, L., Makar, P. A., Martin, R. V., Veefkind, J. P., and Yang, K.: Improved satellite retrievals of $NO_2$ and $SO_2$ over the Canadian oil sands and comparisons with surface measurements, Atmos. Chem. Phys., 14, 3637–3656, doi:10.5194/acp-14-3637-2014, 2014.

Nadirov, R. K., Syzdykova, L. I., Zhussupova, A. K., and Usserbaev, M. T.: Recovery of value metals from copper smelter slag by ammonium chloride treatment, Int. J. Miner. Proc., 124, 145–149, doi:10.1016/j.minpro.2013.07.009, 2013.

Pougatchev, N., August, T., Calbet, X., Hultberg, T., Oduleye, O., Schlüssel, P., Stiller, B., St. Germain, K., and Bingham, G.: IASI temperature and water vapor retrievals – error assessment and validation, Atmos. Chem. Phys., 9, 6453–6458, doi:10.5194/acp-9-6453-2009, 2009.

Prodanova, M., Perez, J. L., Syrakov, D., San Jose, R., Ganev, K., Miloshev, N., and Roglev, S.: Application of mathematical models to simulate an extreme air pollution episode in the Bulgarian city of Stara Zagora, Appl. Math. Model., 32, 1607–1619, doi:10.1016/j.apm.2007.05.002, 2008.

Psiloglou, a. E., Larissi, I. K., Petrakis, I., Paliatsos, A. G., Antoniou, n., and Viras, L. G.: Case studies on summertime measurements of $O_3$, $NO_2$, and $SO_2$ with a DOAS system in an urban semi-industrial region in Athens, Greece, Environ. Monit. Assess., 185, 7763–7774, doi:10.1007/s10661-013-3134-2, 2013.

Rastmanesh, F., Moore, F., Kharrati-Kopaei, M., and Behrouz, M.: Monitoring deterioration of vegetation cover in the vicinity of smelting industry, using statistical methods and TM and ETM+ imageries, Sarcheshmeh copper complex, Central Iran, Environ. Monit. Assess., 163, 397–410, doi:10.1007/s10661-009-0843-7, 2010.

Rastmanesh, F., Moore, F., Kharrati Kopaei, M., Keshavarzi, B., and Behrouz, M.: Heavy metal enrichment of soil in Sarcheshmeh copper complex, Kerman, Iran, Environ. Earth Sci., 62, 329–336, doi:10.1007/s12665-010-0526-2, 2011.

Realmuto, V. J. and Watson, I. M.: Advances in thermal infrared mapping of volcanic sulfur dioxide, EOS Trans, AGU, 82, 47, 2001.

Rix, M., Valks, P., Hao, N., van Geffen, J., Clerbaux, C., Clarisse, L., Coheur, P.-F., Loyola R., D. G., Erbertseder, T., Zimmer, W., and Emmadi, S.: Satellite Monitoring of Volcanic Sulfur Dioxide Emissions for Early Warning of Volcanic Hazards, IEEE J. Sel. Top. Appl. Earth Obs. Rem. S., 2, 196–206, doi:10.1109/jstars.2009.2031120, 2009.

Rodgers, C. D.: Inverse Methods for Atmospheric Sounding: Theory and Practice, World scientific, Singapore, 2000.

Say, N. P.: Lignite-fired thermal power plants and $SO_2$ pollution in Turkey, Energy Policy, 34, 2690–2701, doi:10.1016/j.enpol.2005.03.006, 2006.

Schlüssel, P., Hultberg, T. H., Phillips, P. L., August, T., and Calbet, X.: The operational IASI Level 2 processor, Adv. Space Res., 36, 982–988, doi:10.1016/j.asr.2005.03.008, 2005.

Schmidt, A., Leadbetter, S., Theys, N., Carboni, E., Witham, C. S., Stevenson, J. A., Birch, C. E., Thordarson, T., Turnock, S., Barsotti, S., Delaney, L., Feng, W., Grainger, R. G., Hort, M. C., Höskuldsson, Á., Ialongo, I., Ilyinskaya, E., Jóhannsson, T., Kenny, P., Mather, T. A., Richards, N. A. D., and Shepherd, J.: Satellite detection, long-range transport and air quality impacts of volcanic sulfur dioxide from the 2014–2015 flood lava eruption at Bardarbunga (Iceland), J. Geophys. Res.-Atmos., 120, 9739–9757, doi:10.1002/2015JD023638, 2015.

Smith, R. J.: Use and Misuse of the Reduced Major Axis for Line-Fitting, Am. J. Phys. Anthropol., 140, 476–486, doi:10.1002/ajpa.21090, 2009.

Smith, S. J., van Aardenne, J., Klimont, Z., Andres, R. J., Volke, A., and Delgado Arias, S.: Anthropogenic sulfur dioxide emissions: 1850–2005, Atmos. Chem. Phys., 11, 1101–1116, doi:10.5194/acp-11-1101-2011, 2011.

Stebel, K., Amigo, A., Thomas, H., and Prata, A.: First estimates of fumarolic $SO_2$ fluxes from Putana volcano, Chile, using an ultraviolet imaging camera, J. Volcanol. Geoth. Res., 300, 112–120, doi:10.1016/j.jvolgeores.2014.12.021, 2015.

Stevenson, D. S., Johnson, C. E., Collins, W. J., and Derwent, R. G.: The Atmospheric Sulphur Cycle and the role of Volcanic $SO_2$, Geol. Soc. Lond. Spec. Publ., 213, 295–305, doi:10.1144/GSL.SP.2003.213.01.18, 2003.

Tamburello, G., Aiuppa, A., McGonigle, A. J. S., Allard, P., Cannata, A., Giudice, G., Kantzas, E. P., and Pering, T. D.: Periodic volcanic degassing behavior: The Mount Etna example, Geophys. Res. Lett., 40, 4818–4822, doi:10.1002/grl.50924, 2013.

Tassi, F., Aguilera, F., Vaselli, O., Darrah, T., and Medina, E.: Gas discharges from four remote volcanoes in northern Chile (Putana, Olca, Irruputuncu and Alitar): a geochemical survey, Ann. Geophys., 54, 121–136, doi:10.4401/ag-5173, 2011.

Theys, N., De Smedt, I., van Gent, J., Danckaert, T., Wang, T., Hendrick, F., Stavrakou, T., Bauduin, S., Clarisse, L., Li, C., Krotkov, N., Yu, H., Brenot, H. and Van Roozendael, M.: Sulfur dioxide vertical column DOAS retrievals from the Ozone Monitoring Instrument: Global observations and comparison to ground-based and satellite data, J. Geophys. Res.-Atmos., 120, 2470–2491, doi:10.1002/2014jd022657, 2015.

Van Damme, M., Clarisse, L., Heald, C. L., Hurtmans, D., Ngadi, Y., Clerbaux, C., Dolman, A. J., Erisman, J. W., and Coheur, P. F.: Global distributions, time series and error characterization of atmospheric ammonia ($NH_3$) from IASI satellite observations, Atmos. Chem. Phys., 14, 2905–2922, doi:10.5194/acp-14-2905-2014, 2014.

Vardar, N. and Yumurtaci, Z.: Emissions estimation for lignite-fired power plants in Turkey, Energy Policy, 38, 243–252, doi:10.1016/j.enpol.2009.09.011, 2010.

Varley, N. R. and Taran, Y.: Degassing processes of Popocatepetl and Volcan de Colima, Mexico, Geol. Soc. Lond. Spec. Publ., 213, 263–280, doi:10.1144/gsl.sp.2003.213.01.16, 2003.

Walker, J. C., Dudhia, A., and Carboni, E.: An effective method for the detection of trace species demonstrated using the MetOp Infrared Atmospheric Sounding Interferometer, Atmos. Meas. Tech., 4, 1567–1580, doi:10.5194/amt-4-1567-2011, 2011.

Wang, T.: Emission characteristics of CO, $NO_x$, $SO_2$ and indications of biomass burning observed at a rural site in eastern China, J. Geophys. Res., 107, ACH 9-1–ACH 9-10, doi:10.1029/2001jd000724, 2002.

Wang, T., Hendrick, F., Wang, P., Tang, G., Clémer, K., Yu, H., Fayt, C., Hermans, C., Gielen, C., Müller, J.-F., Pinardi, G., Theys, N., Brenot, H., and Van Roozendael, M.: Evaluation of tropospheric $SO_2$ retrieved from MAX-DOAS measurements in Xianghe, China, Atmos. Chem. Phys., 14, 11149–11164, doi:10.5194/acp-14-11149-2014, 2014.

Watson, I., Realmuto, V., Rose, W., Prata, A., Bluth, G., Gu, Y., Bader, C., and Yu, T.: Thermal infrared remote sensing of volcanic emissions using the moderate resolution imaging spectroradiometer, J. Volcanol. Geoth. Res., 135, 75–89, doi:10.1016/j.jvolgeores.2003.12.017, 2004.

Wesely, M. L.: Parameterization of surface resistances to gaseous dry deposition in regional-scale numerical models, Atmos. Environ., 41, S52–S63, doi:10.1016/j.atmosenv.2007.10.058, 2007.

Xu, W. Y., Zhao, C. S., Ran, L., Lin, W. L., Yan, P., and Xu, X. B.: $SO_2$ noontime-peak phenomenon in the North China Plain, Atmos. Chem. Phys., 14, 7757–7768, doi:10.5194/acp-14-7757-2014, 2014.